Title
Understanding interface stability in solid-state batteries

Journal
Nature Reviews Materials, 5(2)

ISSN
2058-8437

Authors
Xiao, Yihan
Wang, Yan
Bo, Shou-Hang
et al.

Publication Date
2020-02-15

DOI
10.1038/s41578-019-0157-5

Peer reviewed

Understanding of interface stability in solid-state batteries resubmission version 09/30/2019

Yihan Xiao[1,2], Yan Wang[3], Shou-Hang Bo[2,4], Jae Chul Kim[2,5], Lincoln J. Miara[3], and Gerbrand Ceder[1,2,*]

[1]Department of Materials Science and Engineering, University of California Berkeley, Berkeley, CA 94720, United States
[2]Materials Sciences Division, Lawrence Berkeley National Laboratory, Berkeley, CA 94720, United States
[3]Advanced Materials Lab, Samsung Research America, 3 Van de Graaff Dr., Burlington, MA 01803, United States
[4]University of Michigan – Shanghai Jiao Tong University Joint Institute, Shanghai Jiao Tong University, Minhang District, Shanghai 200240, P.R. China
[5]Department of Chemical Engineering and Materials Science, Stevens Institute of Technology, Hoboken, NJ 07030, United States
[*]To whom correspondence should be addressed. Email: gceder@berkeley.edu

Abstract

Solid-state batteries (SSBs) using a solid electrolyte show potential for providing improved safety as well as higher energy and power density compared with conventional Li-ion batteries. However, two critical bottlenecks remain: the development of solid electrolytes with ionic conductivities comparable to or higher than those of conventional liquid electrolytes and the creation of stable interfaces between SSB components, including the active material, solid electrolyte, and conductive additives. Although the first goal has been achieved in several solid ionic conductors, the high impedance at various solid/solid interfaces remains a challenge. Recently, computational models based on *ab initio* calculations have successfully predicted the stability of solid electrolytes in various systems. In addition, a large amount of experimental

data has been accumulated for different interfaces in SSBs. In this review, we summarize the experimental findings for various classes of solid electrolytes and relate them to computational predictions, with the aim of providing a deeper understanding of the interfacial reactions and insight for the future design and engineering of interfaces in SSBs. We found that in general, the electrochemical stability and interfacial reaction products can be captured with a small set of chemical and physical principles.

1 Introduction

Rechargeable Li-ion batteries (LIBs) have revolutionized the energy storage market and enabled the widespread use of portable electronic devices and electric vehicles. Replacing the liquid electrolyte in conventional LIBs with a solid electrolyte (SE) can further improve their energy densities and safety by reducing flammability, improving the cycle life, and enabling the use of alkali-metal anodes. Unlike currently used organic liquid electrolytes, inorganic solid-state conductors are non-flammable or have much higher onset temperatures for thermal runaway. The reactivity of liquid electrolytes with electrodes also contributes significantly to the capacity fade of the battery[1,2]. Such electrolyte decomposition can in principle be mitigated by selecting an inorganic material that is thermodynamically stable or can passivate further reactions with electrodes. Indeed, minimal capacity fade over 10,000 cycles was observed in a solid-state cell employing a thin-film lithium phosphorus oxynitride (LiPON) electrolyte[3]. SEs may also enable the use of lithium or sodium metal anodes, which have much higher volumetric and gravimetric capacities than graphite or hard carbon[4,5]. In liquid electrolyte, the formation of metal dendrites can short-circuit the cell[6,7]. In contrast, some SEs have shown the potential to suppress this dendrite formation[3,8,9], but the general effectiveness of ceramics in preventing

dendrite growth between the electrodes remains in question[10,11].

The development of solid-state batteries (SSBs) has in part been limited by the lack of solid materials with room-temperature ionic conductivities comparable to those of liquid electrolytes. However, this issue has recently been overcome. The room-temperature conductivity of $LiPF_6$ and $NaPF_6$ in the liquid solvent ethylene carbonate:dimethyl carbonate (EC:DMC) is 5–10 mS cm^{-1}.[12,13] Recently, several SEs have exhibited comparable or higher ionic conductivity with a Li-ion transference number close to 1 (compared with values often below 0.5 in liquid electrolytes[12]). These superionic conductors include the Na superionic conductor (NASICON)-type oxides[14–19], lithium and sodium β-alumina[20–23], lithium garnets[24–27], perovskites[28], and antiperovskites[29]. Sulfides, including thio-Li superionic conductor (LISICON)-type compounds $Li_{4-x}M_{1-x}P_xS_4$ (M=Ge, Si)[30,31], $Li_{10}GeP_2S_{12}$ (LGPS)[32] and its derivatives[33,34], Li_2S–P_2S_5 glass[35] and $Li_7P_3S_{11}$ glass-ceramic[36], and argyrodites Li_6PS_5X (X = Cl, Br, I)[37,38], constitute another large family of superionic conductors. To date, the highest room-temperature Li-ion conductivity reported in an SE is 25 mS cm^{-1} in LGPS-type $Li_{9.54}Si_{1.74}P_{1.44}S_{11.7}Cl_{0.3}$[33]. High ionic conductivity has also been achieved in Na-ion sulfides such as Na_3PS_4[39,40], Na_3PSe_4[41], Na_3SbS_4[42], and $Na_{10}SnP_2S_{12}$[43,44] as well as in alkali closo-borates[45,46].

Although remarkable improvements have been made in achieving high bulk ionic conductivities in SEs, this high conductivity is often negated by the high impedance at the interface between the SE and electrode. The interfacial impedance can dominate the internal resistance in a battery and is a particularly prominent issue for SSBs that pair sulfide electrolytes with high-voltage oxide cathodes[47–50]. On the anode side, reactions between the strongly reducing alkali metal and SE can also cause high internal resistance[51,52]. These reactions can occur during both battery cycling and processing. The latter is especially common in oxide SEs as high

processing temperatures[24] and co-sintering with the cathode are typically required to achieve intimate interfacial contact[53–55]. A number of strategies have been developed to mitigate these interfacial reactions, most commonly the use of a buffer layer between the electrode and SE[56–58].

In this review, we examine the phenomena observed experimentally at these critical solid/solid interfaces in SSBs for different types of SEs and relate them to theoretical predictions and understanding based on various models for the interfacial kinetics. Although the prediction of the exact reaction products at the interface remains challenging because of the complex interplay between the thermodynamic and kinetic factors, the computational methods have shown success in predicting the possible decomposition products, providing bounds for electrochemical stability windows, revealing trends in chemical reactivity, and guiding the interface engineering. We focus on the interface stability issues involving a wide range of commonly investigated SEs, namely sulfides, garnets, LiPON, perovskites, antiperovskites and NASICONs, as well as inorganic coating materials. We note that although interfacial phenomena such as dendrite formation[10,59], mechanical issues resulting from volume change in the electrode[60], and poor wetting between the electrode and SE[61,62] also play a critical role in determining the performance of SSBs, they are beyond the scope of this review.

2 Interfaces in SSBs

Each interface in SSBs can be categorized into one of three main classes according to its stability, following the numbering convention outlined by Wenzel et al.[52,63]:

Type I - Thermodynamically stable interface with no driving force for reactions.

Type II - Reacting to form a non-passivating interphase with both electronic and ionic conductivity, denoted as mixed ionic–electronic conducting interphase (MCI).

Type III - Reacting to form a stable solid electrolyte interphase (SEI) with negligible electronic conductivity, limiting further reaction.

Long-term stable battery performance can only be expected for type I (stable) and type III (passivating) interfaces. For the latter, the ionic conductivity of the SEI is critical for battery performance.

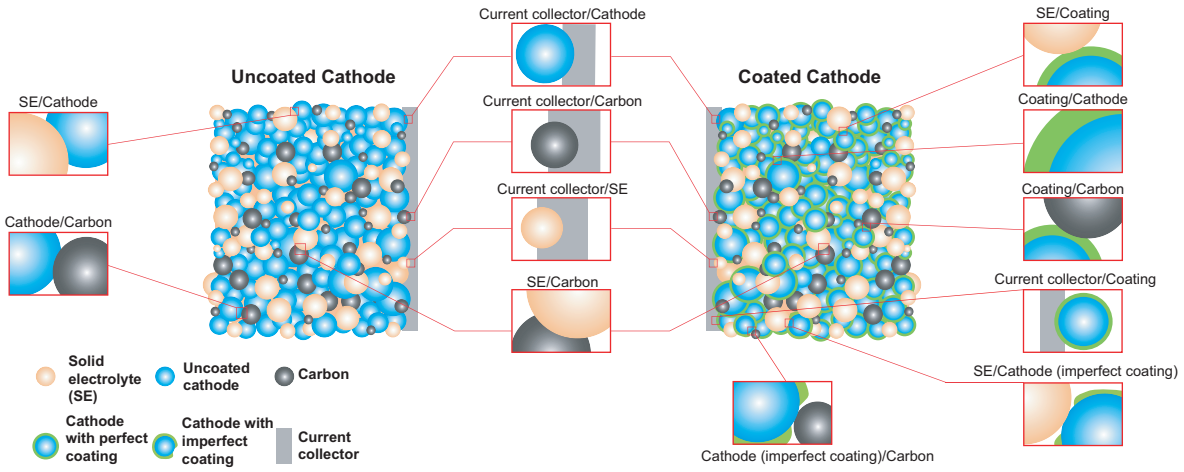

Figure 1: **Various interfaces in cathode composites of SSBs with and without cathode coating.**

Fig. 1 schematically illustrates the wide variety of interfaces present in cathode composites with coated and uncoated active cathode materials. Most studies focus on the cathode/SE interface as good ion transport across this interface must be maintained at all times. Thermodynamic stability at this interface is difficult to maintain because of the narrow electrochemical stability windows of many SEs and their non-negligible chemical reactivity with the cathode. Specifically, because the active cathode material must also allow the transport of electrons, the SE in contact with the cathode particle is subjected to the alkali chemical potential set by the cathode voltage. When the SE is not thermodynamically stable at such a high voltage, it tends to decompose into phases often with reduced ionic conductivity. For example, sulfide elec-

trolytes are predicted to undergo oxidation above ~2.5 V vs. Li metal[64–66] and decompose into phases with lower or even no lithium content[64]. Additionally, the interdiffusion of element(s) and chemical reaction between the SE and cathode can also generate phases that impede ion conduction across the interface[47,66].

One strategy used to satisfy the stringent stability requirement is the use of an electronically insulating but ionically conducting electrode coating. The addition of such a coating layer creates two new interfaces: one between the coating and electrode material and the other between the coating and SE. Because the coating acts as a second electrolyte, it must be stable at the electrode voltage and resist chemical reactions with both the electrode and SE. However, if coating layer imperfections leave part of the electrode surface in contact with the SE, as shown in Fig. 1, unfavorable interfacial reactions will still occur in the coated electrode system. On the other hand, these coating imperfections may be necessary for the electron transport between the coated electrode and current collector, posing a paradox in the current coating strategy[67].

Among the remaining interfaces in cathode composites, decomposition of the SE can also occur at the current collector/SE and carbon/SE interfaces, where the SE is subjected to the working lithium or sodium chemical potential[68–70]. Although neither ion nor electron transport across these interfaces is required for battery cycling, such decomposition would unavoidably compromise the high bulk ionic conductivity of the SE over time.

On the alkali–metal anode side, the instability of the SE arises from its reduction by metallic lithium or sodium. If the SE contains a metal or metalloid element(s), such reduction often leads to the generation of electron conductive products at this interface, rendering it a detrimental MCI that will continuously consume the SE[52,63,64].

3 Interface models

Direct experimental probing of buried solid/solid interfaces is fundamentally challenging, as it is difficult to separate the solids for experimental characterization without damaging their surfaces[71]. Focused ion beam (FIB) milling has been used to create cross sections of such interfaces for characterization with transmission electron microscopy (TEM) or energy-dispersive X-ray spectroscopy (EDX) analysis[47,72]. The decomposition of a perovskite SE or LiPON during Li deposition has also been successfully investigated using *in situ* X-ray photoelectron spectroscopy (XPS)[63,73]. The experimental difficulty of characterizing the interface has motivated the computational modeling of these interfaces using density functional theory (DFT). These computational methods differ in the kinetic limitations they impose, the assumptions made about the effects of external conditions (e.g., electrochemical cycling, high-temperature processing), and the extent of intermixing possible at the interface. We discuss the various levels at which interface stability can be modeled as they can give insight into the products experimentally observed at the interfaces.

3.1 Electrochemical stability (Fast kinetics)

The *electrochemical stability window* or *voltage stability window* of an SE describes its ability to resist oxidation or reduction through the extraction or insertion of alkali ions and electrons. Because a high operating voltage is desirable for batteries with high energy density, the SE must be stable over a wide voltage window. It should be noted that although the electrochemical stability window is an intrinsic property of the bulk SE instead of an interface, it is critical to the interface stability because the electrochemical decomposition of the SE typically occurs at its interface with an electron source, where the SE directly experiences the applied voltage.

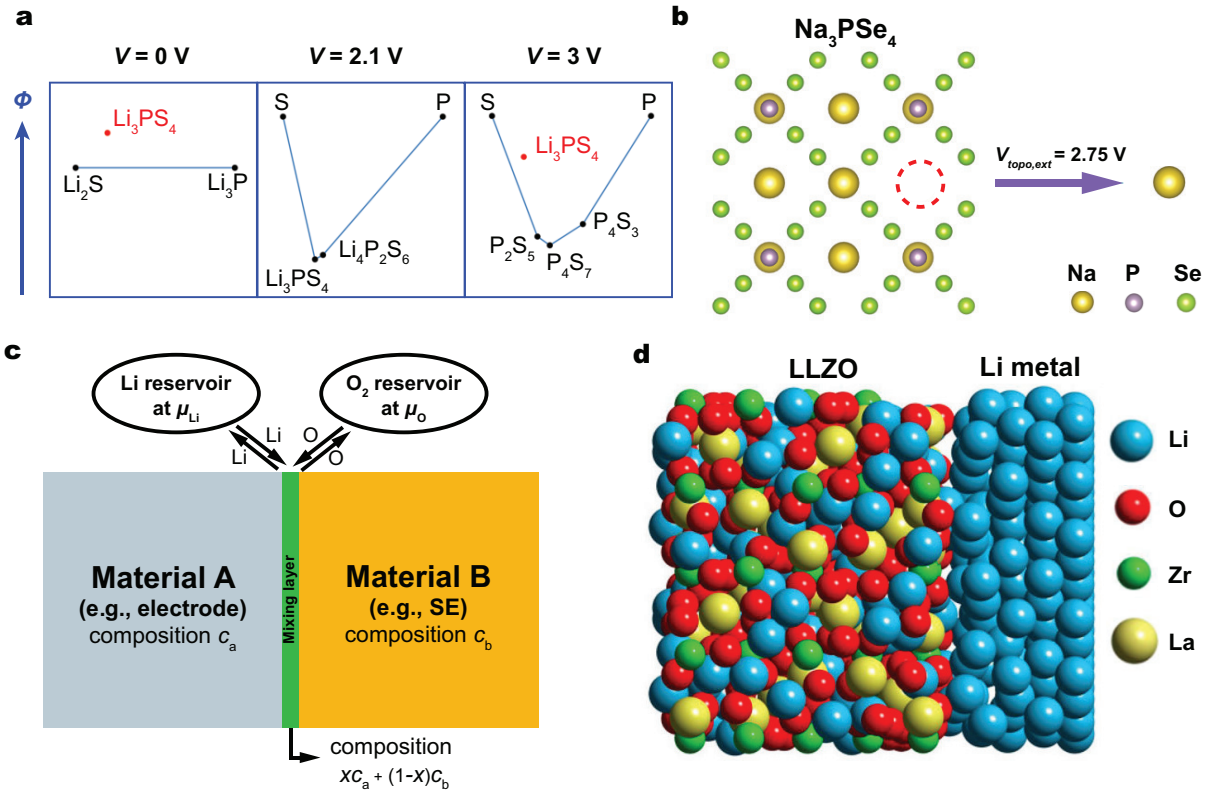

Figure 2: **Interface models for the evaluation of (electro)chemical stability. a** | Grand potential (Φ) convex hulls of the Li–P–S system at voltage $V = 0$ V (left), 2.1 V (middle), and 3 V (right) vs. Li metal. The x-axis gives the composition of P along the pseudo-binary S–P tie line. Note that the Li amount in each compound is variable as it is equilibrated with the voltage (chemical potential). β-Li_3PS_4 is colored red when it is metastable. **b** | Topotactic extraction voltage ($V_{topo,ext}$) of a Na_3PSe_4 SE determined by calculating the energy cost for extracting one Na atom from the SE[50]. **c** | Schematic illustration of chemical mixing at the interface between material A (grey) and material B (orange). The mixing layer (green) at the interface may have an arbitrary mixing fraction x of material A. The interface system can be modeled as open to the external chemical potential of an element such as lithium or oxygen. **d** | Explicit atomistic model of the low-energy LLZO(001)/Li(001) interface. Panel **d** is adapted with permission from REF.[74].

The applied voltage V can be directly converted to an alkali (e.g., Li) chemical potential μ_{Li} using Equation 1[75] neglecting overpotential effects, where μ_{Li}^{o} is the lithium chemical potential in Li metal and e is the elementary charge:

$$\mu_{Li} = \mu_{Li}^{o} - eV. \tag{1}$$

Hence, at the cathode side, the SE experiences a very low Li chemical potential and is subject to decomposition by Li extraction. Formally, such stability can be evaluated by calculating the grand potential Φ of the material using Equation 2, where c is the composition of the material, $E[c]$ is the enthalpy, and $n_{Li}[c]$ is the Li concentration of composition c:

$$\Phi[c, \mu_{Li}] = E[c] - n_{Li}[c]\mu_{Li} = E[c] - n_{Li}[c]\mu_{Li}^{o} + n_{Li}[c]eV. \tag{2}$$

The grand potential convex hull at a given voltage, V, is formed by the grand potentials of a set of phases and their linear combinations that minimize the grand potential at each composition $c - n_{Li}$ that excludes Li. The electrochemical stability window of a material corresponds to the range of voltage over which it is stable (exactly on the grand potential convex hull). As an example, three grand potential convex hulls containing the SE β-Li_3PS_4 at different voltages are presented in Fig. 2a. It can be observed that β-Li_3PS_4 is thermodynamically stable at 2.1 V but not at 0 V and 3 V.

Decomposition of an SE yields new phases, which may require an activated process such as nucleation and thus an overpotential. For instance, the breakdown of an SE at high voltage (i.e., decomposition by oxidation) is predicted to form phases with lower Li content (e.g., P_2S_5 for

β-Li_3PS_4 at $V = 3$ V). Therefore, the stability estimated from this grand potential convex hull method represents the worst-case scenario (i.e., no kinetic stabilization) for the SE. Although it is difficult to directly predict such nucleation overpotentials, they should be similar to those observed in conversion electrodes (typically no more than a few hundred millivolts)[76,77].

3.2 Topotactic stability

Although the thermodynamic approach in the previous section provides the *narrowest* electrochemical stability window, the maximum voltage limits for an SE can be estimated from the potentials at which an electron and an alkali ion can be topotactically removed or added, as this process is expected to have no kinetic limitations: electron extraction/addition should be facile at the interface and an SE has by definition high bulk ionic mobility, and the facile transfer of alkali ions across the interface is assumed. The calculation of this topotactic stability window is analogous to the calculation of battery voltages in intercalation electrodes[75,78]. Fig. 2b presents an example of the calculation of the topotactic extraction voltage ($V_{topo,ext}$) for the Na SE Na_3PSe_4, where the voltage to extract the most unstable Na atom from the SE was calculated to be 2.75 V using Equation 3. Here, μ^o_{Na} is the Na chemical potential in Na metal and $E[c - \mathrm{Na}]$ is the enthalpy of a relaxed supercell with the highest energy Na atom removed topotactically.

$$V_{topo,ext} = (E[c - \mathrm{Na}] + \mu^o_{Na} - E[c])/e \tag{3}$$

Because no nucleation of new phases or diffusion of any element besides mobile alkali atoms is required, such oxidation and reduction decomposition reactions cannot be prevented by kinetic stabilization. Therefore, the topotactic stability method provides the *widest* electrochemical

stability window and an estimate of the best-case scenario (i.e., the maximum degree of kinetic stabilization) for the SE.

3.3 Reactivity associated with chemical mixing

When considering the electrochemical stability, as in the previous sections, one only considers that the alkali element crosses the interface. However, at some interfaces (e.g., between the SE and cathode), chemical reaction may also occur via the mixing of other elements across the interface. Such chemical reactivity between the SE and electrode material has been observed after cycling at room temperature[60,79], and is particularly important at elevated temperature when the electrode and SE need to be co-sintered to achieve intimate contact between particles[80–82] and when the cathode and coating are annealed[83]. Predicting the exact reaction pathway that will occur between two materials at such an interface is difficult as it depends on the complex balance between thermodynamic driving forces and kinetically accessible mechanisms at the reaction temperature, most of which cannot currently be quantified. Instead, computational methods have focused on capturing the maximal chemical driving force that can exist at an interface and the possible reaction products. At a minimum, this thermodynamic analysis can be used to classify interfaces according to their degree of reactivity. The reaction between two solids A and B, with respective compositions c_a and c_b, at their common interface may consume an arbitrary amount of each phase, such that the average composition of the interfacial products is not known *a priori* (Fig. 2c). Richards et al.[64] proposed a method to estimate the reactivity by determining at which fraction of A and B the reaction driving force becomes maximal. Thus, given the phase diagram and energy landscape of the joint chemical space of

A and B, the thermodynamic reactivity is calculated by minimizing

$$\Delta E[c_a, c_b] = E_{\text{pd}}[xc_a + (1-x)c_b] - xE[c_a] - (1-x)E[c_b] \tag{4}$$

over x, where E_{pd} is the lowest energy combination of the reaction products at composition $xc_a + (1-x)c_b$. The relevant energies calculated by DFT in these large chemical spaces can be obtained from databases such as the Materials Project[84], and the ability to find the minimum is now an explicit feature in the Materials Project[85]. Extension to Equation 4 can easily be made by evaluating the grand potential under open-system conditions for an alkali element (to study the chemical reactivity under an applied voltage) or oxygen (to study the reactivity under high-temperature condition) at a certain chemical potential[64]. This methodology has been used to investigate the chemical compatibility of high-voltage spinel cathodes against garnets and NASICONs during sintering[82].

3.4 Explicit interface calculations

For the previous methodologies, the reaction free energies are all treated as those of bulk solids, consistent with the fact that reaction energies are typically very large, making it reasonable to neglect the effect of interfacial energies in the reaction driving force. It is also possible to directly assess the energetics of species at the interface (either statically or dynamically) using DFT on supercells that model the interface explicitly. Interfaces with explicit structural relaxations have been examined in several systems, including Li_3PS_4/Li[86], LLZO/Li and Li_2CO_3/Li[62,74], $LiCoO_2$/Li_3PS_4 and $LiNbO_3$/Li_3PS_4[87], $LiCrS_2$/Li_3PS_4 and $LiMnS_2$/Li_3PS_4[88], and LiPON/Li[89]. For example, Sharafi et al. performed DFT structural relaxations of LLZO/Li and Li_2CO_3/Li interfaces to evaluate their wetting property[74]. The optimized atomic struc-

ture of the low-energy interface LLZO(001)/Li(001) is shown in Fig. 2d. Compared with the results of the previous methodologies based on the bulk energies, those from explicit interface calculations are sensitive to the starting configuration of the interface system. In addition, it is important to understand that the structural relaxation method only optimizes the atomic coordinates locally at the interface and cannot account for any activated process such as the atomic diffusion or the nucleation of new solids.

Interfaces for $LiFePO_4$ ($FePO_4$)/Li_3PS_4[90], $Li_7P_3S_{11}$/Li, $Li_{10}GeP_2S_{12}$/Li, β-Li_3PS_4/Li[91], and $NaCoO_2$/Na_3PS_4[92] have been modeled using *ab initio* molecular dynamics (AIMD). AIMD simulation of the interface has a high computational cost and typically only captures the dynamics of the system at elevated temperatures and very small time scales (< 1 ns). Hence, it should always be combined with a thermodynamic assessment of the possible reaction products.

In the following sections, we relate results obtained using these computational methods to experimental observations in interface systems involving various classes of SEs.

4 Sulfides

Sulfides, especially thio-phosphates based on the Li–P–S system, have emerged as leading SE candidates because of their high ionic conductivities. In addition, their solution processability and ability to deform under cold pressing provide sulfides with an advantage for cell manufacturing compared with oxides. Examples of sulfide SEs with high ionic conductivity include the thio-LISICON conductor $Li_{3.25}Ge_{0.25}P_{0.75}S_4$ (2.2 mS cm^{-1})[30], $Li_{10}GeP_2S_{12}$ (LGPS, 12 mS cm^{-1})[32], $Li_7P_3S_{11}$ glass-ceramic (17 mS cm^{-1})[36], and nanoporous β-Li_3PS_4 (0.16 mS cm^{-1})[93].

Despite the high ionic conductivity of sulfide SEs, their lack of interfacial stability in SSBs remains a pressing issue. Although electrochemical stability windows of sulfides from 0 V to

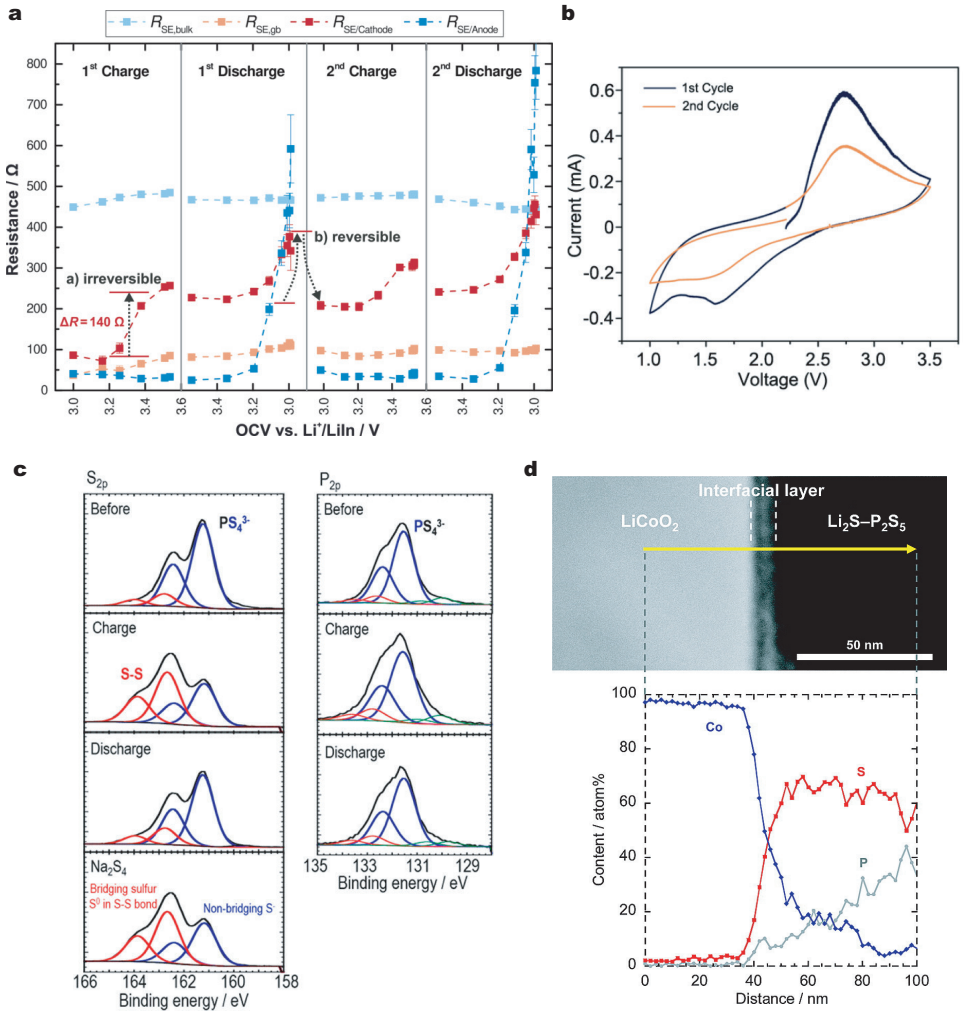

Figure 3: **(Electro)chemical instability of sulfide SEs. a** | Evolution of four components of the resistance in a Li–In|β–Li_3PS_4|NCM–811/β–Li_3PS_4 cell obtained by fitting the impedance spectra in the first and second cycle as a function of the OCV. **b** | CV of a Li|LGPS|LGPS+C|Pt cell between 1.0 and 3.5 V. **c** | P 2p and S 2p XPS spectra of the Li_3PS_4 glass+carbon composite electrode before and after charge–discharge processes. **d** | (Top) Cross-sectional HAADF-STEM image of the $LiCoO_2$ electrode/Li_2S–P_2S_5 interface after the first charge and (bottom) cross-sectional EDX line profiles for Co, P, and S elements. Panel **a** is reproduced with permission from REF.[60]. Panel **b** is reproduced with permission from REF.[94]. Panel **c** is reproduced with permission from REF.[95]. Panel **d** is reproduced with permission from REF.[47].

more than 4 V (vs. Li metal) have been claimed in many studies based on cyclic voltammetry (CV) measurements[30,32,36,93,96], DFT calculations predicted the propensity for S^{2-} to oxidize at approximately 2–2.5 V[64–66]. Furthermore, SSBs employing sulfide SEs often exhibit a large first-cycle capacity loss and subsequent capacity fade of approximately 1%–2% per cycle[60,97].

Such poor capacity retention can be partly attributed to the high and growing interfacial resistance between the sulfide SE and electrode (or carbon), which has been observed in both theoretical modeling and carefully designed electrochemical measurements. Using electrochemical impedance spectroscopy, the variation of the resistance of a β-Li_3PS_4-based solid-state cell with the open-circuit voltage (OCV) has been separated into different origins (Fig. 3a)[60]. It has been demonstrated that a large and irreversible interfacial resistance was built up at the cathode/sulfide SE interface upon the first charge, with the most drastic increase occurring between 3.2 and 3.4 V. This high interfacial resistance at the cathode/sulfide SE interface can be understood by considering the narrow DFT-calculated electrochemical stability windows of sulfides between 1.5 and 2.5 V[64–66,98,99], above which the oxidation decomposition of sulfides would occur. For example, LGPS is predicted to have an electrochemical stability window of 1.7–2.1 V[66] or 2.1–2.3 V[64], both of which are much narrower than the stability limits claimed from CV measurements. The pitfalls of CV measurements will be discussed in detail in section 7.2. The discrepancy between the CV measurements and *ab initio* predictions was reconciled by Han et al.[100], who added carbon (C) to LGPS to increase the active area (i.e., the contact area between LGPS and an electron conductor) for the charge-transfer reaction, thus increasing the extent of the decomposition reaction. Fig. 3b presents the CV result of a Li|LGPS|LGPS+C|Pt cell between 1.0 V and 3.5 V, which clearly shows the oxidation of LGPS starting at approximately 2.1 V[94,100]. Using the same method, a reduction potential of LGPS at 1.7 V was also

observed[100]. These measured oxidation and reduction limits are in excellent agreement with the DFT-predicted values, contrary to previous experimental reports[32]. In a different attempt, Tian et al. mixed a Na SE and carbon to determine its electrochemical stability window by slow galvanostatic charging and discharging in a liquid cell and monitoring the voltage–capacity profiles[50]. The resulting windows of 0.9–2.5 V and 1.25–2.35 V for Na_3PS_4 and Na_3PSe_4, respectively, are also in reasonably good agreement with the theoretical predictions (1.55–2.25 V for Na_3PS_4 and 1.80–2.15 V for Na_3PSe_4)[50].

The work by Han et al.[100] highlights the role of electronically conductive additives such as carbon in the SE decomposition: The SE decomposition at high voltage is a pure electrochemical process as it can occur at the SE/carbon interface where the SE provides the Li-ion path and carbon provides the electron path. At this interface, electrochemical oxidation of the sulfides occurs instead of reduction, as would be expected from a purely chemical reaction with carbon. These insights further highlight a serious problem associated with SSBs: although adding conductive additives, such as carbon, to the cathode composite is common, decomposition of the SE will occur everywhere the SE contacts the electron path (current collector, conductive additive). Even though this degradation may not be immediately visible in the short-term performance of the cell, as this interface is not along the Li-ion or electron transport path to the cathode particles, continued degradation of the SE from this interface will ultimately impair the Li-ion conductivity and lead to the performance decay, as observed with long-term cycling of sulfide-based cells[68,69]. Severe oxidation of β-Li_3PS_4 on the current collector has also been observed experimentally[70]. This problem can only be resolved by creating a passivating interface between the SE and electron path or by minimizing the addition of the conductive additive to the cathode composite.

The narrow stability window of LGPS has been further confirmed by the low voltage of a battery made solely from LGPS as both the active electrode materials and SE[94]. In line with the predicted low oxidation voltage for sulfides, *operando* XPS measurements indicated the onset of Li_2S–P_2S_5 oxidation at approximately 2.7 V[101]. Sn-substituted LGPS, $Li_{10}SnP_2S_{12}$[34,102], has a similar narrow predicted stability window (1.78–2.02 V)[43]. Indeed, Tarhouchi et al. determined an electrochemical stability window of 1.5–2.5 V for $Li_{10}SnP_2S_{12}$ from CV measurements with a three-electrode setup, where a lithium counter electrode was not used to avoid side reactions[103].

Fairly good consistency between experimental and computational results has also been observed for the oxidation decomposition products of sulfide SEs. The predicted oxidation products for Li_2S–P_2S_5 include elemental sulfur[64–66] and more condensed sulfides with lower Li content such as P_2S_5[65,66], $Li_4P_2S_6$, and P_2S_7[64] as well as GeS_2 for LGPS[64–66]. In experiments, P_2S_5 was not directly observed using XPS; however, oxidized sulfur species with S–S bonds have been detected at the $LiNi_{0.8}Co_{0.1}Mn_{0.1}O_2$/$\beta$-$Li_3PS_4$ interface[60,70], possibly indicating the presence of elemental sulfur. Similar bridging of S–S bonds between PS_4 groups has been observed at the Li_3PS_4 glass/carbon interface after charging to 3.6 V[95]. Swamy et al. charged a β-Li_3PS_4+carbon cathode to 5 V and observed the formation of elemental sulfur[104], further confirming that S^{2-} in sulfide SEs oxidizes at high voltages. For LGPS, the formation of GeS_2-like species and $Li_2P_2S_6$ has been observed in a cathode composite containing LGPS after extended cycling[68,105].

Notably, recent studies showed that the decomposition of several sulfide SEs may be partially reversible or the decomposition products are redox-active, although it is unlikely that these processes would contribute to the long-term cycling capacity of a battery. Hakari et al. observed the association/dissociation of S–S bonds in a Li_3PS_4 glass+carbon cathode compos-

ite upon cycling between 0.6 and 3.6 V by tracking the XPS peak assigned to the bridging S–S bond (Fig. 3c)[95]. The XPS result combined with Raman and X-ray absorption fine structure (XANES) data suggests that PS_4 groups in the Li_3PS_4 glass undergo condensation upon charging and the process is partially reversible upon discharging[95]. This finding appears to be consistent with the reversible and potential-dependent change of the interfacial resistance of the cathode[70]. Using CV on a Li|β-Li_3PS_4|β-Li_3PS_4+C cell between 0 and 5 V, Swamy et al. showed that the decomposition of β-Li_3PS_4 at 5 V is irreversible but with good reversibility observed for subsequent cycles, indicating that the decomposition products are redox-active in this voltage range[104]. They further demonstrated that this redox activity is a superposition of that from elemental sulfur and phosphorus.

In addition to the electrochemical stability limitation of sulfides, the sulfide/oxide cathode interface suffers from the degradation resulting from chemical mixing. As observed in the cross-sectional scanning TEM (STEM) image of a charged $LiCoO_2$/Li_2S–P_2S_5 interface and associated EDX line profile in Fig. 3d, the interfacial layer contains Co, P, and S, with Co diffusing into Li_2S–P_2S_5 for over 50 nm[47]. Consistent with this observation, the computed driving force for chemical reaction between sulfides and oxide cathodes is large (> 300 meV/atom), forming transition-metal sulfides (e.g., Co_9S_8[66], Mn_2S_3[64], Ni_3S_4[64], and $CoNi_2S_4$[85]) and PO_4^{3-} and SO_4^{2-} polyanions[64,66,99,106]. The formation of PO_4^{3-} and transition-metal sulfides results from the exchange of S^{2-} in PS_4^{3-} from the SE with O^{2-} from the cathode. This exchange is energetically favorable as the bond energy is significantly higher for a P–O bond than for a P–S bond but similar for transition metal–sulfur and transition metal–oxygen bonds[107]. Consistent with the thermodynamically predicted products, Haruyama et al. explicitly modeled the $LiCoO_2$/β-Li_3PS_4 interface and observed that the energetically favorable exchange of Co and P leads to

the formation of P–O and Co–S bonds[87]. Not surprisingly, when pairing sulfide SEs with sulfide cathodes containing the same S^{2-} anion chemistry (e.g., $LiCrS_2$, $LiMnS_2$, or $LiTiS_2$), the sulfide cathode/sulfide SE interfaces are much more stable than the oxide cathode/sulfide SE interfaces, as observed from chemical mixing calculations[64] and in explicit interface calculations[88]. In the same spirit, thio-phosphate SEs were predicted to be chemically more compatible with $LiFePO_4$ containing the same P^{5+} cation than with other oxide cathodes such as $LiCoO_2$ and $LiMn_2O_4$[67].

For experiments performed at room temperature, severe chemical mixing between sulfide SEs and oxide cathodes appears to occur only after charging and long cycling[60]. No reactivity has been observed between the as-prepared $LiNi_{0.8}Co_{0.1}Mn_{0.1}O_2$ and β-Li_3PS_4; however, after the first charge, PO_x^{y-} species were detected at the interface using XPS[60]. After 100 cycles, time-of-flight secondary ion mass spectrometry (ToF-SIMS) analysis revealed the formation of various PO_x^{y-} and SO_x^{y-} groups at the $LiNi_{0.8}Co_{0.15}Al_{0.05}O_2/Li_2S$–$P_2S_5$ interface[79]. The effect of charging and cycling on chemical mixing may be explained by the fact that the computed chemical reactivity with a sulfide SE is even more pronounced for charged cathodes than for discharged compounds[66]. High-temperature processing can also promote the chemical mixing at the oxide cathode/sulfide SE interface. Tsukasaki et al. heated the charged $LiNi_{1/3}Mn_{1/3}Co_{1/3}O_2$ with 75 Li_2S–25 P_2S_5 glass above 300 °C and observed transition-metal sulfides MnS and $CoNi_2S_4$, and Li_3PO_4 using synchrotron X-ray diffraction (XRD) and TEM[108], in excellent agreement with the predicted reaction products at that interface[85]. Similar products and the exchange between O^{2-} and S^{2-} (or Se^{2-}) have been predicted by calculations on Na sulfide and selenide SEs with oxide cathodes[50]. Indeed, sodium transition-metal sulfides (or selenides) and Na_3PS_3O have been observed using XRD at elevated temperature for a mixture of $NaCrO_2$ and Na_3PS_4 (or

Na_3PSe_4)[50].

The reduction decomposition of sulfide SEs is typically initiated by the reduction of P^{5+} and other cations (e.g., Ge^{4+}, Sn^{4+}) into phases including $Li_4P_2S_6$[64], P[65,66], and Li_2S. Upon contacting Li metal, they further decompose into a metal, Li–metal alloys and/or Li-containing binary compounds such as Li_3P[65,66]. For example, Li_3PS_4 and $Li_7P_3S_{11}$ have been predicted to decompose into Li_3P and Li_2S when in contact with a Li metal anode[64,86,99]. The predicted decomposition is similar for LGPS, with additional germanium reduction to form $Li_{15}Ge_4$[64,98]. The formation of a metal or Li–metal alloy (as in the LGPS case) at the SE/Li interface is considered detrimental as it makes the interphase an MCI, leading to the continued decomposition of the SE. The pronounced driving force to form these products makes them appear in AIMD simulations of crystalline Li–P–S compounds or LGPS in contact with Li metal. Even within 20 ps at 300 K, the formation of Li_xS, Li_yP, and Li_zGe species is indicated by the lithium coordination numbers of S, P and Ge at the end of the simulation[91]. Indeed, Raman spectroscopy and XPS analyses have revealed the conversion of PS_4^{3-} in β-Li_3PS_4 to $P_2S_6^{4-}$ and Li_2S at the β-Li_3PS_4/gold interface upon Li deposition as well as partial reversibility upon Li stripping[109]. The detected $P_2S_6^{4-}$ species is consistent with the predicted $Li_4P_2S_6$ formation at the onset of reduction[64]. Li_2S, Li_3P, and other reduced phosphorus species were detected at the $Li_7P_3S_{11}$/Li interface using XPS and XRD[110], and additionally reduced Ge (likely Li–Ge alloy or Ge) at the LGPS/Li interface[52]. As a result of the MCI formation, the LGPS/Li interface suffers from the continuous decomposition and resistance growth[52,111]. A similar phenomenon has been reported for $Li_{10}SiP_2S_{12}$ and $Li_{10}Si_{0.3}Sn_{0.7}P_2S_{12}$ in contact with Li[112], where the electronically conductive $Li_{17}Sn_4$ and $Li_{21}Si_5$ phases are predicted to form[34].

In contrast, many lithium–nonmetal binary phases are stable against Li metal[64]. In princi-

ple, these binaries are good candidates for passivating the SE/Li interface if they are ionically conductive but electronically insulating. For example, to stabilize the Li_2S–P_2S_5 glass/Li interface, LiI was added to the glass SE[113], enabling the stable cycling of a Li symmetric cell[9,111,113]. A similar effect has been achieved in Na_3PS_4, where Cl doping has been shown to improve capacity retention by introducing the electron insulator NaCl at the Na_3PS_4/Na interface[114]. Another Na-ion conductor Na_3SbS_4 has been predicted and experimentally verified to form Na_2S and Na_3Sb at its interface with Na metal, making the interphase an MCI. One solution was proposed by Tian et al.[115] who purposely exposed Na_3SbS_4 to air to generate a hydrated $Na_3SbS_4{\cdot}8H_2O$ phase on its surface, which, upon contacting Na metal, produced Na-stable compounds NaH and Na_2O with good ionic conductivity and high electronic resistivity[115]. This hydration process has been shown to effectively passivate the SE/Na interface and enable more stable cycling of a Na symmetric cell. These findings highlight the effectiveness of introducing ionic conductive but electronic insulating phases to the SEI as well as the importance of predictive calculations in the reverse design of battery interfaces.

Argyrodites with the general chemical formula Li_6PS_5X (X = Cl, Br, I) are another class of sulfide ionic conductors[37,38] that are predicted to have a similar electrochemical window, chemical reactivity with cathodes, and decomposition products to other sulfides[64,116]. Consistent with the predictions[64,65,116], elemental sulfur, lithium polysulfide, P_2S_x, and LiCl have been observed to be the oxidation decomposition products[117,118]. For argyrodites in contact with Li metal, the decomposition products Li_2S and Li_3P have been detected by XPS[119]. Recently, Walther et al. investigated the interface between $LiNi_{0.6}Co_{0.2}Mn_{0.2}O_2$ and Li_6PS_5Cl using XPS and ToF-SIMS[120]. Similar to the observation at the $LiNi_{0.8}Co_{0.1}Mn_{0.1}O_2/\beta$-$Li_3PS_4$ interface[79], increased amounts of PO_x^{y-} and SO_x^{y-} species were detected upon cycling[120]. The

presence of the halide anion also leads to the generation of LiX (X=halogen) binaries upon decomposition, which may assist in passivating the interfaces with the electrode as for Cl-doped Na_3PS_4[114]. Indeed, good capacity retention over 300 cycles has been reported in a $LiNi_{1/3}Co_{1/3}Mn_{1/3}O_2|Li_6PS_5Cl|Li–In$ cell[118]. Doping Li_6PS_5Br with O has also been shown to improve the stability against Li metal and oxide cathodes[64–66,121].

In summary, although sulfide materials combine excellent mechanical processability and ionic conductivity, experimental and theoretical investigations indicate that their chemical and electrochemical stability are severely limited. First, the facile oxidation of S^{2-} results in poor electrochemical stability limited to approximately 2.5 V in the cathode composite. S^{2-} oxidation leads to condensation of PS_4 units with a general decrease of Li content and ultimately even to the elemental sulfur formation. Such oxidation decomposition is considered one of the main causes of the large first-cycle capacity loss in a high-voltage solid-state cell[60]. Although this degradation is mostly considered to occur at the cathode/SE interface, it occurs even at non-functional interfaces such as the carbon/SE and current collector/SE interfaces. This degradation will reduce the effective ionic conductivity in the cathode composite. Because the SE decomposition products that form at high voltage are generally highly oxidized and alkali-deficient, they may retard further decomposition; however, the extent to which these decomposition products are passivating requires further investigation. Second, when oxide cathodes are in contact with sulfide SEs, there is a further driving force for degradation via the exchange of S^{2-} and O^{2-}, leading to the formation of PO_4^{3-} polyanions and transition-metal sulfides. This effect will lead to both impedance growth and capacity loss.

Against the Li metal anode, reduction of all but just a few metal or metalloid ions will occur and create electronically conducting products that form an MCI. This phenomenon is a

particular problem for some highly conducting sulfides that contain Ge, Si, Sn, and Sb. The addition of halogens, such as I and Cl, may contribute to the formation of a passivating SEI containing Li halides that prevents further reduction.

5 Oxides

Oxide-based SEs include garnets, thin-film LiPON, perovskites, antiperovskites, and NASICONs. They exhibit higher oxidation stability as well as improved chemical stability with oxide cathodes compared with sulfide SEs[64–66]. However, the room-temperature bulk ionic conductivity of oxide SEs is generally lower than sulfides, and their large grain-boundary resistance further restricts the total ionic conductivity[17,122–125]. Because of the mechanical rigidity of oxides, high-temperature sintering is usually required to produce a dense SE pellet and to achieve intimate contact between the SE and electrode within the electrode composite[24,55,125,126]. The high processing temperature can degrade electrode materials such as $LiNi_xCo_yMn_{1-x-y}O_2$ (NCM)[127] and $LiCoO_2$[128] and promote the chemical reactivity at the SE/electrode interface[82,129]. The difficulty of cell manufacturing with oxide SEs results in limited reports on the performance of full solid-state cells with a thick electrode composite layer and a dense oxide SE pellet[130,131], yielding fewer experimental data on the interfacial stability of oxide SEs under battery operating conditions than those of sulfide SEs.

5.1 Garnets

Among oxide SEs, lithium garnets have been widely studied because of their high ionic conductivity (10^{-4}–10^{-3} S cm^{-1}[24,25,27,132]), apparent stability against lithium metal, and wider electrochemical windows than sulfides[24–26,133,134]. The first reported Li-ion conducting garnets

had the composition $Li_5La_3M_2O_{12}$ (M = Nb, Ta) (LLNbO, LLTaO)[135]. Since then, strategies to increase the Li concentration via aliovalent doping have been used to achieve higher ionic conductivity in garnets, including subvalent doping with a 2+ ion on the La^{3+} site or another transition-metal cation on the M^{5+} site[24]. The highest ionic conductivity has been achieved for cubic $Li_7La_3Zr_2O_{12}$ (LLZO) and its derivatives[24,25,27,136,137]. It should be noted that a contamination layer containing LiOH and Li_2CO_3 has been observed on the surface of the garnet upon exposure to air, resulting in poor wetting with Li metal and thus a high resistance at the garnet/Li interface[61,138,139]. Methods to improve the wetting and physical contact between the garnet and electrode have been covered in several recent reviews[140,141].

The oxidation stability of garnet SEs has been investigated using CV measurements[26,144–146]. Similar to those for sulfides, early CV measurements also claimed significantly wider electrochemical stability windows (0–5 V) than DFT-predicted results (e.g., 0.05–2.9[100] or 0.07–3.2 V[64] for LLZO). Recently, Han et al. prepared a Li|LLZO|LLZO+C|Pt cell in an Ar atmosphere and observed the onset of oxidation at ~4.0 V in CV[100]. Similarly, an oxidation current above 3.7 V was detected in the CV of a Li|Ta-doped LLZO (LLZTO)|(LLZTO+C) cell (Fig. 4a)[142]. In both studies, with the addition of carbon to increase the reaction region, better agreement with the predicted oxidation limit of LLZO (2.9 or 3.2 V[64,65]) was observed than for the previous CV measurements[100,142]. Jalem et al. claimed from DFT calculation that carbon may have participated in the oxidation of LLZO at high voltage to form Li_2CO_3 and/or CO_2, although no clear experimental evidence was obtained[142].

The reduction stability of garnets depends on the transition-metal cation in the composition, as it determines the energy of the orbital for electron insertion upon reduction. According to DFT calculations, the intrinsic reduction limits for LLZO, LLTaO, and LLNbO are 0.05

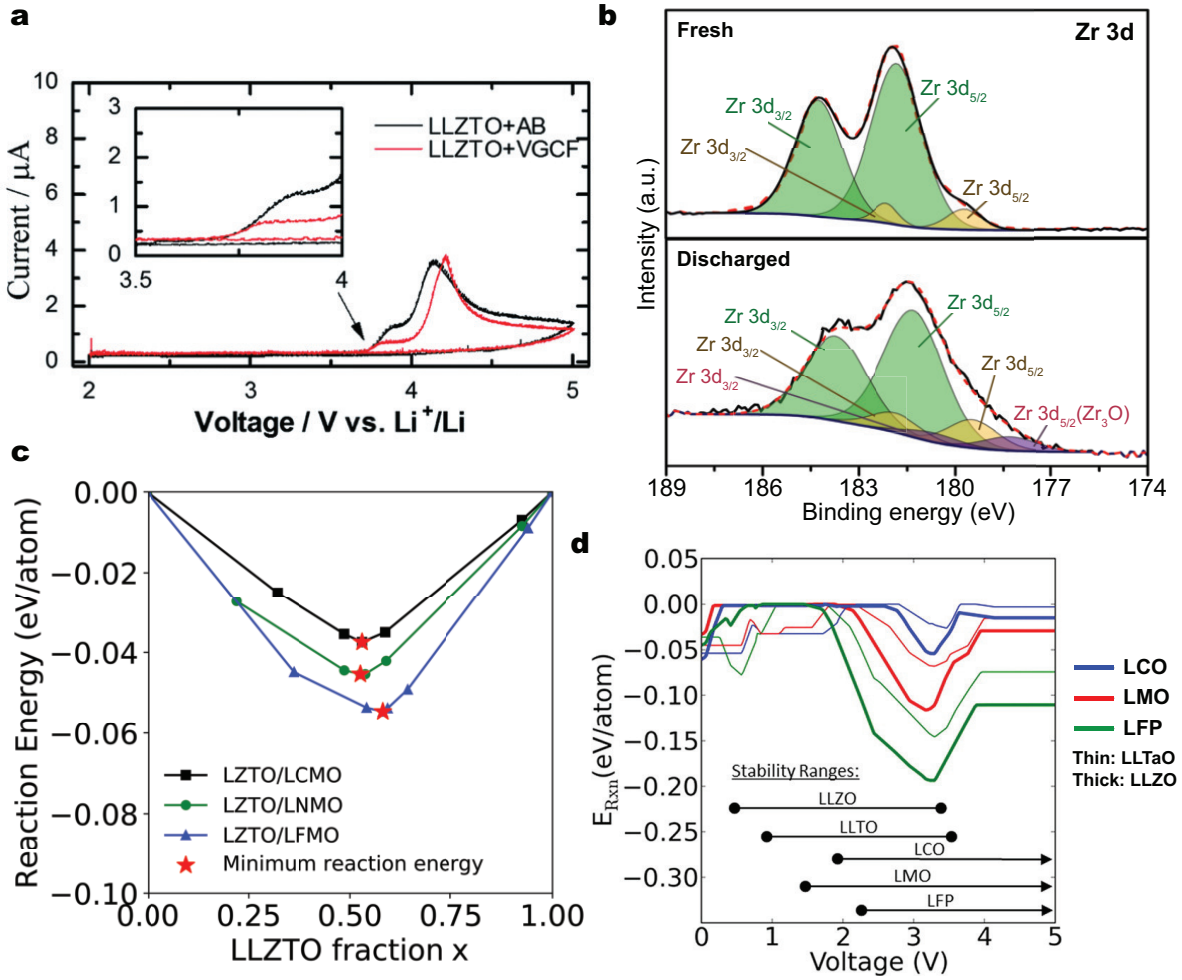

Figure 4: **(Electro)chemical instability of garnet SEs. a** | CV of Li|LLZTO|(LLZTO+C) cells. AB: acetylene black, VGCF: vapor-grown carbon fiber. **b** | High-resolution Zr 3d core XPS spectra of fresh and discharged (to 0 V vs. Li metal) LLZO. The new peak after discharging at 178.2 eV is attributed to Zr_3O. **c** | Reaction energy between spinel cathodes and LLZTO at 800 °C; the minimum reaction energy is denoted by the red star. LCMO: $LiCoMnO_4$, LNMO: $Li_2NiMn_3O_8$, LFMO: $Li_2FeMn_3O_8$. **d** | Reaction energy for chemical mixing between the garnet SE (LLTaO or LLZO) and cathode, with voltage varying from 0 to 5 V vs. Li metal. Note that the intrinsic instability for reactants at the given voltage is excluded. LCO: $LiCoO_2$, LMO: $LiMn_2O_4$, LFP: $LiFePO_4$. The calculated intrinsic stability windows are marked along the bottom for reference. Panel **a** is reproduced with permission from REF.[142]. Panel **b** is reproduced with permission from REF.[100]. Panel **c** are adapted with permission from REF.[82]. Panel **d** is adapted with permission from REF.[143].

(or 0.07) V[64,65], 0.85 V[143], and 1.05 V[85], respectively, indicating that the cation reducibility increases as Zr^{4+}<Ta^{5+}<Nb^{5+}. LLZO was computed to be only marginally unstable against Li metal with a driving force for reduction decomposition of 20 meV/atom[66], and the possible reduction products include Zr, La_2O_3, Li_8ZrO_6, Zr_3O, and Li_2O[64–66]. Such a small driving force may not be sufficient to nucleate the solid products, which may lead to a kinetically stabilized LLZO/Li interface. The kinetic stability of garnets against Li metal can also be evaluated by considering the Li insertion into the garnet structure during the initial reduction process. Nakayama et al. calculated using DFT that the topotactic lithium insertion voltages of LLZO and LLTaO are –0.95 V and –1.03 V, respectively[147], indicating that initiating the reduction of LLZO and LLTaO requires a high activation energy. In contrast, the computed topotactic lithium insertion voltage for LLNbO is positive (0.07 V), which suggests the facile reduction of LLNbO by Li metal[147].

Experimental observations at the garnet/Li interfaces agree well with the DFT calculations. Early studies involving contacting a garnet pellet with molten Li and observing the color change suggested that LLZO and LLTaO may be stable against Li metal[25,136,144,148] whereas LLNbO is not stable, likely because of the reduction of the Nb^{5+} cation[149]. The impedance of a Li|$Li_{6.25}La_3Zr_{1.25}Nb_{0.75}O_{12}$|Li symmetric cell was observed to increase with time[149] and cycle number[150]; however, that of a symmetric cell using LLZO or $Li_{6.25}La_3Zr_{1.25}Ta_{0.75}O_{12}$[150–152] did not increase. Several studies using XRD and XPS analyses also revealed no detectable structural or oxidation state change in LLZO and LLTaO upon contacting Li[144,148,153,154], confirming the apparent stability of LLZO/Li and LLTaO/Li interfaces.

Despite the predicted high kinetic barrier for LLZO reduction[147], the reactivity at the LLZO/Li interface can be revealed by elevating the reaction temperature, thereby accelerating

the reaction kinetics, or using advanced characterization techniques which allow minimal reactions to be detected. Wolfenstine et al. heated Al-doped LLZO samples in molten Li at 300–350 °C and indeed observed the chemical coloration of the LLZO surface[154]. *In situ* STEM characterization of the LLZO/Li interface indicated that Zr^{4+} was slightly reduced when contacting Li metal, producing a ~6-nm-thick tetragonal LLZO interphase[155]. DFT calculations have shown that the tetragonal phase is lower in energy than the cubic phase at higher Li concentration[155], suggesting that the formation of the tetragonal LLZO layer is caused by Li insertion into the cubic LLZO. Han et al. confirmed the reduction of Zr^{4+} to one of the predicted decomposition products, Zr_3O[65], after discharging to 0 V in a Li|liquid electrolyte|LLZO+C half cell; the associated XPS results are presented in Fig. 4b[100]. Very recently, Zhu et al. studied the effect of dopants (Nb, Ta, Al) in LLZO on its stability with Li metal[156]. Similar to the previous findings, the XPS data indicated that Nb^{5+} is reduced by Li metal, leading to the formation of an MCI and causing a continuously increase of the interfacial impedance with time. These researchers also observed some Zr^{4+} reduction to Zr^{2+} or Zr^0 in all three doped samples. Other reducible dopants such as Fe^{3+} in LLZO also leads to strong reduction at the LLZO/Li interface, resulting in the formation of a thick (130 μm) tetragonal LLZO interphase and a large interfacial resistance[157].

The chemical stability of garnets against different cathodes has been investigated using DFT[64,66,82,143]. The stability of the garnet/cathode interface at elevated temperature is important as sintering is typically required for oxide SE processing[24]. The predicted driving force for LLZO reaction with $LiCoO_2$ and $LiNi_{1/3}Co_{1/3}Mn_{1/3}O_2$ at 0 K is extremely low (1 meV/atom) but higher for $LiMn_2O_4$ (63 meV/atom) and $LiFePO_4$ (94 meV/atom)[66,67]. However, at high temperature, configurational entropy may further favor interdiffusion of elements between the

SE and cathode, increasing the interfacial chemical reactivity. Li loss above 1000 °C[158] and the generally more reducing environment at high temperature[82,159] may also shift the system to off-stoichiometry and induce instability of garnets. For instance, the decomposition products $La_2Zr_2O_7$ and La_2O_3 have been observed in LLZO thin films sintered at 1090 °C and 1100 °C[160]. These two products are also predicted to form when charged $Li_{0.5}CoO_2$ is brought in contact with LLZO or when LLZO is oxidized at high voltage[66], indicating that the formation of these products are driven by the loss of Li from LLZO.

The results of several experimental characterization studies of the LLZO/cathode interface at high temperature are consistent with the thermodynamic predictions. Ren et al. showed with XRD analysis that $LiMn_2O_4$ and $LiFePO_4$ react strongly with LLZTO at 500 °C, whereas $LiCoO_2$ and NCM only showed evidence of a slight reaction with LLZTO to form $LaCoO_3$ at 700 °C detected by XRD and Raman measurements[161]. Similar results were observed for a garnet $Li_6BaLa_2Ta_2O_{12}$ with other oxide cathodes[162]. Furthermore, Tsai et al. reported that no evidence of chemical reaction between $LiCoO_2$ and LLZTO was observed during sintering using Raman analysis[163]. However, conflicting results have been reported. Decomposition products such as La_2CoO_4[80], $La_2Li_{0.5}Co_{0.5}O_4$[164], $La_2Zr_2O_7$[165], and tetragonal LLZO[129] have been observed in different studies of the LLZO/$LiCoO_2$ interface. The formation of tetragonal LLZO was explained by the observed Al diffusion from LLZO to $LiCoO_2$ during sintering, which destabilized the cubic LLZO phase[129]. Zarabian et al. showed that the interdiffusion of La and Co already occurs at 400 °C to form Co_3O_4[81]. Note that the reduced transition-metal cation Co^{2+} is present in both La_2CoO_4 and Co_3O_4, as expected from the reducing environment at high temperature[82]. Miara et al. investigated the reactivity between LLZTO and spinel cathodes using first-principles calculations and experimental characterization[82]. In Fig. 4c, the calculated

reaction energy at 800 °C is plotted as a function of the mixing fraction of LLZTO in the cathode/SE mixture. The minimum reaction energy ranges between –60 and –30 meV/atom, indicating a mild driving force for the decomposition at the garnet/spinel cathode interface at high temperature. The chemical reactivity was verified by XRD analysis, with the detection of reaction products including La_2O_3, $La_2Zr_2O_7$, NiO, Li_2MnO_3, and $LaMnO_3$, in excellent agreement with the DFT prediction. Again, the reduced transition-metal cation (Mn^{3+} in $LaMnO_3$) was observed at high temperature.

During battery cycling, the LLZO/cathode interface is predicted to decompose via chemical mixing[143] or LLZO oxidation as many of the charged cathodes have potentials above the oxidation stability limit of LLZO (2.9 or 3.2 V[64,65]). In Fig. 4d, the computed driving force for chemical mixing between various cathodes and LLZO or LLTaO is plotted as a function of the voltage. Among the reactions between LLZO and three common cathodes $LiCoO_2$, $LiMnO_2$, and $LiFePO_4$ in their typical cycling range of 2.5–4.5 V[129,166], the LLZO/$LiCoO_2$ interface has the lowest driving force for chemical mixing (< ~50 meV/atom), whereas the LLZO/$LiFePO_4$ interface is the most reactive. However, experimental data for garnet/cathode interfaces under battery cycling conditions remain ambiguous. In a $LiCoO_2$|LLZO|Au|Li cell, a small irreversible capacity (~5 mAh g^{-1}) was observed between 2.7 and 3.8 V[129], which is consistent with the predicted LLZO oxidation or chemical mixing with $LiCoO_2$ in this voltage range[66,143]. However, Ohta et al. cycled a solid-state $LiCoO_2$|Nb-doped LLZO (LLZNO)|Li cell (fabricated by depositing a thin film of $LiCoO_2$ on an SE pellet) between 2.5 and 4.2 V at room temperature[167] and reported an excellent first Coulombic efficiency of 99% and capacity retention of 98% after 100 cycles, indicating that the extent of the reactions at both the LLZNO/$LiCoO_2$ and LLZNO/Li interfaces under cycling are small and/or passivating. Therefore, more direct

experimental analysis of the garnet/cathode interface under battery operation is required to determine whether this interface is kinetically stabilized or passivated under long-term cycling.

In summary, although LLZO has often been claimed to be stable with Li metal and to voltages above 5 V, the collective theoretical and experimental data suggest a more nuanced picture. Whereas the Zr-containing garnet only has a minor thermodynamic driving force to react with Li metal, the Nb-containing garnet can clearly be reduced by Li, as evidenced by both DFT calculations and experimental data. Strongly reducible dopants such as Fe^{3+} further deteriorate the reduction stability. The Zr and Ta systems have high barriers for topotactic Li insertion, which likely kinetically stabilize these systems against a Li metal anode. However, if Li insertion occurs in cubic garnets, a tetragonal phase (stabilized by the higher Li content) will form and increase the interfacial impedance. In principle, the slight reduction of Zr^{4+}in LLZO by Li metal would also increase the electronic conductivity of the interphase and slowly propagate into the bulk electrolyte.

The observed oxidation decomposition at approximately 4 V indicates that LLZO cannot be paired with a high-voltage cathode such as $LiNi_{0.5}Mn_{1.5}O_4$ (~4.7 V)[168,169]. Stability investigations with classic layered cathodes such as $LiCoO_2$ and NCM provide a less clear picture. Although Li loss from LLZO, either at high temperature or from extraction from a highly charged cathode, appears to lead to the formation of $La_2Zr_2O_7$ and other cathode-related decomposition products, experimental data indicating the significance of this reaction under normal cycling conditions is missing. In this context, we want to stress that the long-term operation of SSBs will require a very high Coulombic efficiency and that even minor continuing reactivity at the interface must be prevented.

Chemical mixing of garnets with oxide cathodes is much less severe than that for sulfide SEs;

however, the high-temperature sintering required for processing not only destabilizes LLZO by Li loss but also promotes elemental interdiffusion and transition-metal reduction. For example, the reaction products La_2CoO_4 and $LaMnO_3$ both contain a reduced transition-metal cation (Co^{2+} and Mn^{3+}) from the cathode and La^{3+} from the garnet SE. Therefore, techniques such as low-temperature and/or short-time sintering and interfacial modification such as coating are desirable for garnet SEs.

5.2 LiPON

Amorphous lithium phosphorus oxynitride (LiPON) has been successfully used as an SE for thin-film solid-state microbatteries owing to its acceptable ionic conductivity (~10^{-6} S cm^{-1})[170,171], low electronic conductivity (10^{-12}–10^{-14} S cm^{-1})[172,173], and apparent wide electrochemical stability window[8]. Capacity retention of 90% has been observed for a Li/LiPON/$LiNi_{0.5}Mn_{1.5}O_4$ solid-state cell over 10,000 cycles between 3.5 V and 5.1 V[3], with the stability window of LiPON determined using CV ranging from 0 to 5.5 V[8]. Such outstanding electrochemical performance has been used to argue that LiPON is stable against a Li metal anode and possesses excellent high-voltage stability[3,8,170,174]. However, DFT calculations predict the decomposition of LiPON by oxidation of nitrogen above 2.6 V to form N_2 gas and Li_3PO_4 (or $Li_4P_2O_7$), and reduction of phosphorus below 0.68 V to form Li_3P[64–66]. This apparent discrepancy can be explained by the formation of passivating SEIs at both high and low voltage as none of the decomposition products are electron conductive[64,65]. Indeed, gas evolution was observed in a LiPON thin-film cell charged to 5.8 V[8], consistent with the predicted N_2 generation above 2.6 V[65].

When in contact with Li metal, thermodynamic DFT analysis predicts LiPON to be fully reduced to Li_3P, Li_2O, and Li_3N[64]. Explicit interface calculations also point toward the insta-

bility of LiPON against Li metal[89], with Li atoms observed to be inserted into LiPON during the structural relaxation, reducing P^{5+} and breaking P–N and P–O bonds. In experiments, *in situ* XPS analysis performed by Schwöbel et al. indeed revealed the presence of Li_3P, Li_3N, and Li_2O at the LiPON/Li interface[73]. These decomposition products are favorable as they not only block electron conduction but also permit Li-ion diffusion across the interphase[175,176].

The chemical reaction at the LiPON/$LiCoO_2$ interface was investigated using XPS during LiPON sputtering and subsequent annealing[177]. As LiPON was sputtered onto $LiCoO_2$, $LiNO_2$ and likely some Li_2O formed with Co^{3+} being reduced to Co^{2+} in $LiCoO_2$. During the stepwise annealing, $LiNO_2$ disappeared by 300 °C, and Co_3O_4 and Li_3PO_4 formed at higher temperature. This observation agrees well with DFT results predicting Co^{3+} reduction to Co^{2+} and N^{3-} oxidation to N_2 at this interface, with other possible products including CoN, Li_3PO_4, and Li_2O[66]. DFT can also capture interfacial reactions under battery cycling conditions. Using STEM with electron energy loss spectroscopy (EELS), Wang et al. identified a disordered interfacial layer in the pristine $LiCoO_2$/LiPON interface, from which CoO evolved after battery cycling[178]. Indeed, CoO formation was predicted by DFT in the reaction between half-charged $LiCoO_2$ and LiPON[66].

5.3 Perovskites

Perovskite-type lithium lanthanum titanate $Li_{3x}La_{2/3-x}\square_{1/3-2x}TiO_3$ ($0 < x < 0.16$) (LLT) and structurally related materials[28] exhibit high bulk Li-ion conductivity up to ~10^{-3} S cm^{-1} at room temperature[179]. However, the use of LLT as an SE in SSBs is not desirable as it has been observed to form an MCI in contact with Li metal due to the reduction of Ti^{4+}.[28] This phenomenon is consistent with the DFT prediction that LLT decomposes against Li metal into La_2O_3, Li_2O, and metallic Ti_6O[66]. The reduction stability of LLT has been investigated

experimentally by intercalating Li into LLT. The Li intercalation voltage was determined to be 1.8 V using CV[180] and 1.5 V using galvanostatic discharging[181,182], both of which are close to the predicted reduction limit of LLT (1.75 V)[65,66]. X-ray absorption spectroscopy (XAS) analysis of a Li-inserted LLT sample revealed the reduction of Ti from 4+ to 3+, with the La^{3+} valency remaining unchanged as predicted[183,184]. Recently, Wenzel et al. revisited the LLT/Li interface using *in situ* XPS and confirmed the presence of Ti^{3+}, Ti^{2+}, and Ti metal[63].

On the high-voltage side, LLT is predicted to be stable up to 3.71 V and form O_2, TiO_2, and $La_2Ti_2O_7$ at higher voltages[66], indicating that LLT may be paired with low-voltage cathodes such as $LiFePO_4$. Recently, Jiang et al. cycled a Li|LLT|$LiFePO_4$ solid-state cell between 2.8 and 4.0 V, where polyethylene oxide (PEO) was used as the catholyte and also the buffer layer between Li and LLT[184]. The observed high Coulombic efficiency after the first five cycles suggests that LLT oxidation, if any, is self-limiting.

A negligible driving force for chemical mixing of LLT with $LiCoO_2$ (0.5 meV/atom) to form Co_3O_4, $La_2Ti_2O_7$, Li_2TiO_3, and $Li_{0.5}CoO_2$ is predicted using DFT calculations[66]. Indeed, high-resolution TEM analysis revealed that a sharp LLT/$LiCoO_2$ interface was formed using pulsed laser deposition (PLD) without the formation of any intermediate phases[185]. At elevated temperatures, Liao et al. also demonstrated that LLT is chemically stable with $LiMn_2O_4$ up to 800 °C and stable with $LiCoO_2$ up to 700 °C using XRD, although β-LLT was observed in the latter case at a higher temperature[186]. Kotobuki et al. further characterized the decomposition products at the LLT/$LiCoO_2$ interface at 700 °C and detected the formation of Co_3O_4 and $La_2Ti_2O_7$[187], which agrees well with the DFT prediction[66]. In contrast, $LiNiO_2$ was observed to react strongly with LLT to form NiO and $La_2Ti_2O_7$ at 500 °C, which is lower than the reaction onset temperature of 700 °C for $LiCoO_2$[186]. DFT calculations verified that LLT has a higher

reaction driving force with $LiNiO_2$ (17 meV/atom) than with $LiCoO_2$(0.5 meV/atom), and the observed NiO and $La_2Ti_2O_7$ were also predicted to present at the $LiNiO_2$/LLT interface[85].

5.4 Antiperovskites

Li-rich antiperovskites are a class of recently discovered ionic conductors with the basic formula Li_3XY, where X and Y are divalent (e.g., O^{2-}) and monovalent (e.g., Cl^-) anions, respectively. The reported ionic conductivities of antiperovskites range widely from 10^{-7} to 10^{-3} S cm^{-1}.[29,124,188,189]

The most unique feature of antiperovskites is the absence of non-lithium cations in the composition, which in principle leads to an absolute reduction stability at 0 V as no element can be further reduced by Li metal[190]; however, the self-decomposition of metastable Li_3OCl and Li_3OBr into Li_2O and LiCl or LiBr is still possible[190,191]. Lu et al. investigated the Li_3OCl/Li interface by cycling a Li|Li_3OCl thin-film|Li symmetric cell[189]. The voltage of the symmetric cell increased in the first three cycles and then stabilized in subsequent cycles, indicating the apparent stability of Li_3OCl with Li metal. The origin of the initial increase in the cell voltage remains unclear, with one possibility being the Li_3OCl self-decomposition.

On the other hand, the lack of non-lithium cations in the antiperovskites to covalently lower the energy of the anion electron states[192] also limits their oxidation stability to below 3 V. DFT calculations predicted the onset of oxidation of Li_3OCl at 3 V[64] or 2.55 V[190] to form products including ClO_3, $LiClO_3$, $LiClO_4$, Li_2O_2, and LiCl. Because these reaction products are electronic insulators an SEI is expected to form at high voltage and may prevent further SE oxidation. Electrochemical stability windows estimated from CV measurements indicate an oxidation stability of 8 V for the stoichiometric and Ba-doped Li_3OCl[193] and even above 9 V for $Li_2(OH)_{0.9}F_{0.1}Cl$ and Li_2OHBr[194]. These high voltages clearly cannot represent the

intrinsic stability of these conductors but are more likely an indication of the passivation by the SEI formation at the SE/inert electrode interface at high voltage. When pairing Li_3OCl with a $LiCoO_2$ cathode and a graphite anode in a thin-film battery, the Coulombic efficiency in the first cycle is 83% which increased to approximately 95% in the subsequent cycles[189]. Because the computed driving force for chemical mixing between $LiCoO_2$ and Li_3OCl is negligible (7 meV/atom)[85], this phenomenon is more likely to originate from the Li_3OCl oxidation and passivation at high voltage. However, similar to the Li_3OCl/Li interface[189], there is no direct experimental evidence of the interfacial passivation of Li_3OCl at high voltage in the literature, and more careful measurements of the passivation layer and its growth are needed.

5.5 NASICONs

The general formula $Li_{1+x}A_xM_{2-x}(PO_4)_3$, where A is a trivalent cation (e.g., Al^{3+}, La^{3+}, In^{3+}, Cr^{3+}) and M is a tetravalent cation (e.g., Ti^{4+}, Ge^{4+}, Hf^{4+}, Zr^{4+}, Sn^{4+}), represents a class of ionic conductors with the NASICON structure[195]. Two representative compounds in this class, $Li_{1+x}Al_xGe_{2-x}(PO_4)_3$ (LAGP) and $Li_{1+x}Al_xTi_{2-x}(PO_4)_3$ (LATP), have been studied extensively because of their high ionic conductivity ($> 10^{-4}$ S cm^{-1})[17,196,197].

Similar to LLT and LGPS, the Ti^{4+} in LATP and Ge^{4+} in LAGP are expected to undergo facile reduction by Li metal. DFT calculations predict the reduction of LATP and LAGP below 2.17 V (or 2.7 V) and below 2.7 V (or 2.9 V), respectively[64,65], forming $Li_2Ti_2(PO_4)_3$[64], P, $LiTiPO_5$, $AlPO_4$ and Li_3PO_4[65] for LATP, and Ge, GeO_2, $Li_4P_2O_7$ and $AlPO_4$[65] for LAGP. The fully reduced products by Li metal are predicted to be Li_2O, Li_3P, Ti–Al, Li–Al, and Li–Ge alloys[65].

Clearly, the direct contact between LAT(G)P and Li metal cannot lead to stable solid-state cells. Slight but noticeable reduction of LAGP at 0.85 V has been captured by CV[198]. XPS

analysis on the surface of LAGP and LATGP (a commercial NASICON-type glass-ceramic containing both Ti and Ge) after Li deposition revealed Ti^{4+} reduction to Ti^{3+} in LATGP and Ge^{4+} reduction to elemental Ge in LAGP[199], similar to findings for LATGP after cycling in a Li symmetric cell[200]. After contacting LAGP with molten Li, Li–Ge alloy formation has been observed by XPS[201], which is one of the fully reduced products predicted by DFT. However, Al^{3+} remains in its trivalent oxidation state, in contrast to the DFT prediction[65,199]. The presence of electron conductive phases such as Li–Ge alloy at the LAT(G)P/Li metal interface leads to the formation of an MCI, explaining the continuous increase of the impedance of a Li symmetric cell using a LAGP or LATGP SE[199,200]. Further evidence of the reduction decomposition of LAGP was provided by Lewis et al.[202]. Using *in situ* TEM, *ex situ* XRD, SEM, and Raman spectroscopy, they showed that a thick amorphous interphase was formed between Li and LAGP. In addition, the large expansion (130%) of the LATP layer resulting from Li insertion was observed to induce the crack initiation and widening in the LAGP pellet near the LAGP/Li interface[201–203]. Such continuous interfacial-reaction-driven chemomechanical degradation, instead of the interphase formation itself, was claimed to be the primary cause for the observed impedance growth[203].

On the cathode side, LAGP was initially reported to be stable up to 6 V based on CV measurements[204]; however, DFT calculations suggested lower oxidation limits of 4.21 V (or 4.8 V) for LATP and 4.27 V (or 4.5 V) for LAGP, above which O_2 gas and phosphates would form[64,65]. It should be noted that the predicted oxidation stability of LATP and LAGP above 4 V is the highest among all the SEs covered in this review. The high voltage stability can be attributed to the strong P–O hybridization that prevents oxygen oxidation[67].

For LATP in contact with $LiCoO_2$, a mild driving force (~50 meV/atom) is predicted to

delithiate $LiCoO_2$ to $Li_{0.5}CoO_2$ and form Li_3PO_4 in addition to Co_3O_4, $LiAl_5O_8$, and TiO_2[66]. The tendency to form Li_3PO_4 when a compound with PO_4 groups is in contact with a cathode was recently studied in detail[67]. In experiments, the LATGP (or LATP)/$LiCoO_2$ interface remained stable at 500 °C, as indicated by high-resolution TEM analysis[205]; however, interdiffusion occurred at higher temperature, forming a porous amorphous layer. Such high-temperature reactivity has also been observed at LATP/spinel cathode interfaces. Miara et al. used XRD to study the chemical reactivity of mixtures of LATP with different spinel cathodes ($Li_2NiMn_3O_8$, $Li_2FeMn_3O_8$, and $LiCoMnO_4$) at high temperature[82]. Decomposition products including Li_3PO_4, $AlPO_4$, TiO_2, Co_3O_4, $MnFeO_3$, and $LiMnPO_4$ were detected above 600 °C, agreeing well with the DFT-predicted products at this temperature[82]. These results suggest that similar to garnets, NASICON SEs also suffer from severe interface decomposition during the co-sintering process. Under battery operating conditions, no noticeable intermixing was observed at the $LiCoO_2$/LATP interface after 50 cycles in a $LiCoO_2$|LATP|LIPON|Li cell[205], consistent with the calculated zero reaction driving force between LATP and half-lithiated $Li_{0.5}CoO_2$ or fully delithiated CoO_2[66].

A recently developed NASICON-type conductor $LiZr_2(PO_4)_3$ exhibits good ionic conductivity of ~10^{-4} S cm^{-1} at 80 °C[206]. At the $LiZr_2(PO_4)_3$/Li interface, a thin amorphous layer containing Li_3P and Li_8ZrO_6 was formed which likely functions as an SEI due to the poor electronic conductivity[206,207], in contrast to the MCI layers formed at LATP/Li and LAGP/Li interfaces. This comparison highlights the effect of non-lithium cation on the character of the SE/Li interface, which will be detailed in Table 1 in section 7.1. In addition, $LiZr_2(PO_4)_3$ exhibited compatibility with $LiFePO_4$ in a Li/$LiZr_2(PO_4)_3$/$LiFePO_4$ solid-state cell, with a high Coulombic efficiency over 40 cycles[206]. Indeed, $LiZr_2(PO_4)_3$ was calculated to be stable up to

4.60 V and chemically stable with $LiFePO_4$ because of their same anion chemistry[85].

6 Inorganic coatings

Direct contact between the SE and electrode can be avoided by applying a coating layer, which act as an artificial SEI that only permits Li-ion and not electron conduction, thus expanding the practical stability window of the SE. The thickness of the coating can be controlled to be between 1 and 10 nm[47,56,208], which is generally smaller than an *in situ*-formed SEI[47,80,157,202]. The essential requirements for the coating material are the chemical stability with both the SE and relevant electrode, and the electrochemical stability over the operating voltage range of the relevant electrode. Therefore, the composition for the cathode and anode coating should be optimized differently according to the specific SE-electrode combination.

In an early coating demonstration, a $Li_4Ti_5O_{12}$ coating was applied on $LiCoO_2$ to improve the capacity, cyclability, and power density[56]. The application of LiPON coatings on $LiCoO_2$, Li-rich NCM, and $LiNi_{0.5}Mn_{1.5}O_4$ cathodes has also been demonstrated to be effective in enhancing the cyclability at high C-rates and high voltage[209–211]. In addition, $LiNbO_3$ and $LiTaO_3$ are frequently used coating materials because they are relatively easy to coat and exhibit reasonable ionic conductivity when amorphous[57,58]. In fact, $LiNbO_3$, $LiTaO_3$, and $LiNb_{0.5}Ta_{0.5}O_3$ have all shown promise in protecting thio-LISICONs and LGPS from reacting with $LiCoO_2$ and NCM cathodes[32,58,68,212]. Varying degrees of success have also been achieved in SSBs with sulfide SEs using other oxide coatings including Li_2O–ZrO_2[213], Li_2SiO_3[214,215], Li_3BO_3–Li_2CO_3[216], Li_3PO_4[217], $LiInO_2$[218], and Li_2MoO_4[219]. However, the diffusion of Co from $LiCoO_2$ into the oxide coating layer has been observed upon extended cycling[105], leading to the gradual deterioration of the coating in the long term. Although garnets are less reactive than sulfides,

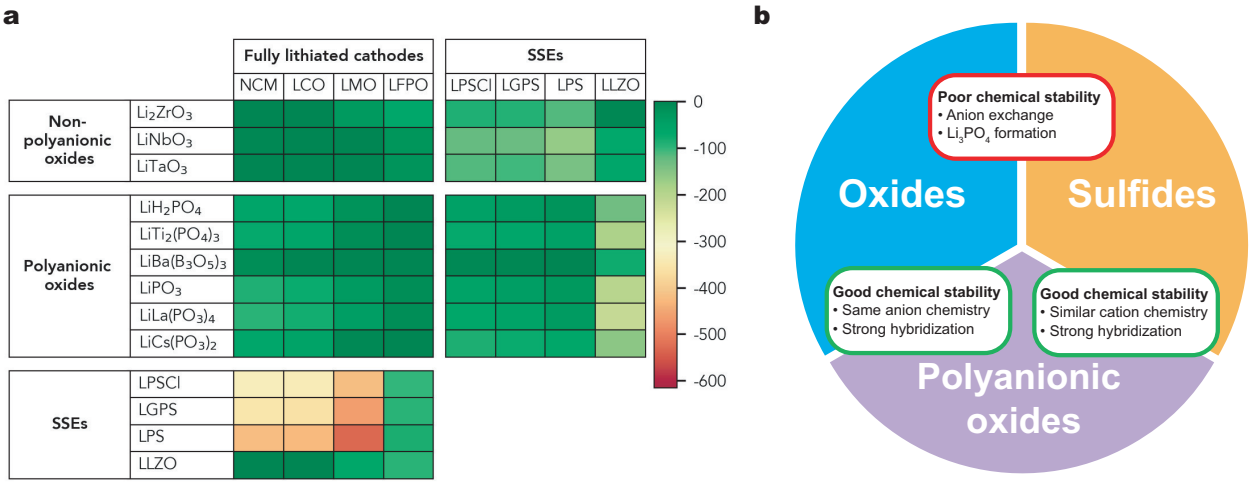

Figure 5: **Polyanionic oxides as a bridge between oxides and sulfides for good chemical compatibility.** **a** | Reaction energies at fully lithiated cathode/SE, fully lithiated cathode/coating, and coating/SE interfaces in meV/atom. Each cell is mapped to a color from green to red according to the color bar on the right. **b**| Pair-wise chemical compatibility between oxides, sulfides, and polyanionic oxides. The red box indicates high reactivity (> 100 meV/atom) and the green boxes indicate low reactivity (< 100 meV/atom). Panel **a** is reproduced with permission from REF.[67].

the reactivity between the garnet and the oxide cathode during high-temperature co-sintering cannot be neglected, as discussed in section 5.1. Glassy Li_3BO_3 with a melting temperature of approximately 700 °C has often been used as a buffer layer to stabilize garnet/cathode interfaces[55,129,220].

The good performance of currently used coating materials can be explained by their wide electrochemical stability window up to ~4 V[166] and reduced reactivity with the oxide cathode and SE[64,66]. However, most of these materials cannot withstand the Li-extraction potential of high-voltage cathodes. For the $LiNbO_3$ and $LiTaO_3$ coatings, a non-trivial driving force (> 100 meV/atom) for chemical mixing still exists between the coating and sulfide SEs[66,67]. A recent high-throughput computational screening considered the electrochemical stability, chemical stability, and ionic conductivity of Li-containing materials[67]. Polyanionic oxides with non-metal–oxygen bonds were shown to be promising cathode coatings, with appealing examples including

LiH_2PO_4, NASICON $LiTi_2(PO_4)_3$, and $LiPO_3$. To illustrate the function of polyanionic compounds as a buffer layer between an oxide cathode and a sulfide SE, Fig. 5a shows the reaction energies of representative (non-polyanionic) oxide and polyanionic oxide coatings with common cathodes and SEs[67]. The oxide cathode/sulfide SE interface suffers from a strong driving force for anion exchange between O^{2-} and S^{2-} to form P–O bonds. In addition, the formation of Li_3PO_4 is highly favorable because of its deep formation energy (–2.767 eV/atom), which destablizes oxide cathodes or oxide coating materials in contact with Li-rich sulfide conductors. In contrast, many polyanionic coatings (e.g., phosphates and borates) exhibit improved chemical stability with both the oxide cathode and sulfide SE, as indicated by the dark green color in the corresponding cells in Fig. 5a. There are two reasons for this stability: 1) the strong orbital hybridization between non-metal and oxygen in the polyanionic group creates strong covalent bonds (e.g., P–O and B–O), which are chemically inert against reaction, and 2) polyanionic oxides such as the phosphates share the same anion (O^{2-}) with oxides and the same cation (P^{5+}) with thio-phosphates, thereby removing the energy gain from anion exchange. The compatibility issues among the polyanionic oxide, oxide and sulfide chemistries are summarized in Fig. 5b. It should be noted that the tendency to form the stable Li_3PO_4 phase still exists when phosphates contact a Li source[67]. Electrochemically, hybridization in polyanionic oxides also lowers the oxygen electron states, boosting the oxidation stability[67]. Indeed, very recently, Yoshinari et al. employed the NASICON $Li_{1.5}Al_{0.5}Ti_{1.5}(PO_4)_3$ as a catholyte between $LiNi_{0.8}Co_{0.1}Mn_{0.1}O_2$ and a β-Li_3PS_4 SE layer in a full cell[131]. The capacity retention was improved compared with directly using β-Li_3PS_4 as the catholyte and the decomposition at the SE/cathode interface was suppressed.

On the anode side, several classes of compounds including oxides, polyanionic oxides, and

nitrides have been used to stabilize the SE/Li interface. Compounds in the Li–Al–O chemical space have provided effective protection for various SEs against Li metal, including $Li_7P_3S_{11}$, LATP, and $Li_7La_{2.75}Ca_{0.25}Zr_{1.75}Nb_{0.25}O_{12}$[62,221,222]. The computed stability window of Li_5AlO_4 is 0.06–3.07 V, suggesting good stability of Al^{3+} against Li metal, which is also consistent with XPS observations at the LAGP/Li interface[199]. In addition, *in situ*-formed polyanionic compounds Li_3PO_4 and LiH_2PO_4 have been used to stabilize the LLZO/Li and LGPS/Li interfaces, respectively[223,224]. DFT predicted that Li_3PO_4 would form Li_3P and Li_2O in contact with Li metal as well as LiH for LiH_2PO_4[85]. These reaction products are passivating and can enable the stable cycling of Li symmetric cells, similar to the LiPON/Li interface. Consistent with these predictions, Li_3P and Li_2O have been detected at the Li_3PO_4/Li interface by XPS[223]. When exploring other anion chemistries for stabilizing the SE from reduction by Li metal, Mo and coworkers discovered that nitrides have the lowest calculated reduction limits compared with other anion chemistries, making nitride chemistry attractive for SE protection on the anode side[225]. Indeed, BN was recently reported to protect the LATP/Li interface[226] and a Li_3BN_2 glass electrolyte has demonstrated good stability with Li metal, as indicated by the stable cycling profile of a Li symmetric cell[227].

7 Discussion

7.1 Trade-offs between ionic conductivity and electrochemical stability

An ideal SE should exhibit high ionic conductivity and interfacial compatibility with both the anode and cathode. In Fig. 6, we show the oxidation and reduction limits, and room-temperature ionic conductivity for various SE categories. The desired combination of ionic conductivity and electrochemical stability is located at the top right corner (oxidation limit =

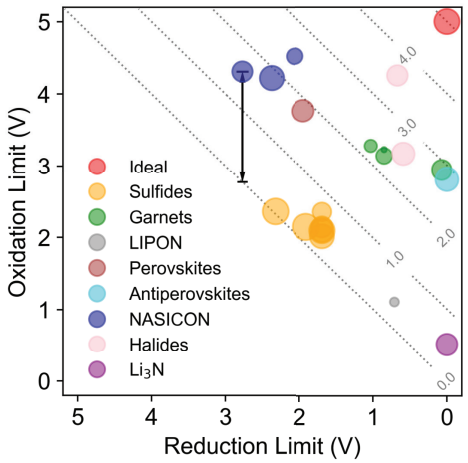

Figure 6: **Electrochemical stability windows of common SEs.** Each SE is represented by a circle with the area proportional to the order of magnitude of its ionic conductivity (in μS cm^{-1}) and the color denoting its category. The stability window is the vertical distance from the center of the circle to the diagonal line, as illustrated by the black arrow. The grey dotted lines are the contours of the width of the stability window.

5 V, reduction limit = 0 V, ionic conductivity = 10 mS cm^{-1}), which has yet to be achieved by any SEs.

Many strategies have been employed to enhance the ionic conductivity or stability of SEs by tuning their compositions. However, as illustrated in Fig. 7, they often result in trade-offs between the ionic conductivity, oxidation and reduction stability, which together prevent the discovery of an ideal SE. For example, the strategy for achieving good ionic conductivity can negatively affect the oxidation stability. Room-temperature Li-ion conductivity above 10 mS cm^{-1} has only been observed in sulfide SEs with the highly polarizable S^{2-} anion, which is excellent at shielding the interactions of Li ions with the host structure or with other Li ions. However, the loosely bonded electrons of S^{2-} are also associated with a low electron affinity and subject to facile electron extraction at high voltage, resulting in an oxidation limit below 2.5 V. In contrast, oxide SEs typically have oxidation limits greater than 3 V (Fig. 6), but the use of O^{2-} comes at the cost of ionic conductivity at least one order of magnitude lower than

that of sulfides because of the reduced shielding effect in oxides[34,228]. This trade-off between the ionic conductivity and oxidation stability in oxides and sulfides has also been investigated from a lattice dynamics perspective in a recent study[229]. Switching the anion chemistry from oxygen and sulfur to halogens such as F^- and Cl^- can make it more difficult to oxidize the anion. In addition, the monovalent anions can reduce the bare electrostatic interaction of Li ions with the anion lattice, but these halogen anions also have a small polarizability, limiting the shielding effect and making the overall effect on the ion mobility unclear at this point[230]. The competition between these two effects depends on the specific structure of the material. There were few halide superionic conductors before the recently reported Li_3YCl_6[231], Li_3YBr_6[231] and Li_3InCl_6[232]. Whether this lack of good halide conductors is intrinsic or a result of the fact that they may be more difficult to synthesize is not yet clear. Hybridizing the anion states may be a viable way to overcome the trade-off between the oxidation stability and ionic conductivity. As discussed in section 6, the hybridization between P (or B) with O in polyanionic coatings lowers the oxygen electron states and increases the oxidation stability compared with those of oxide coatings[67]. This hybridization effect is also demonstrated in Fig. 6, where PO_4-group-containing NASICON conductors (dark blue) exhibit higher oxidation limits than other oxide SEs such as perovskites (brown) and garnets (green). Hybridization may also contribute to the increased ionic conductivity of SEs. Upon substituting Sn with Ge and then with Si in $Li_{10}MP_2S_{12}$ (M=Sn, Ge, Si), the increased hybridization between the M and S elements pulls electron density away from the Li-ion diffusion channel[34,233]. This effect reduces the electrostatic interaction between Li ions and the host structure, leading to a lower Li-ion migration barrier[34,233].

Metals and metalloids make up over 70% of the periodic table. Their introduction into

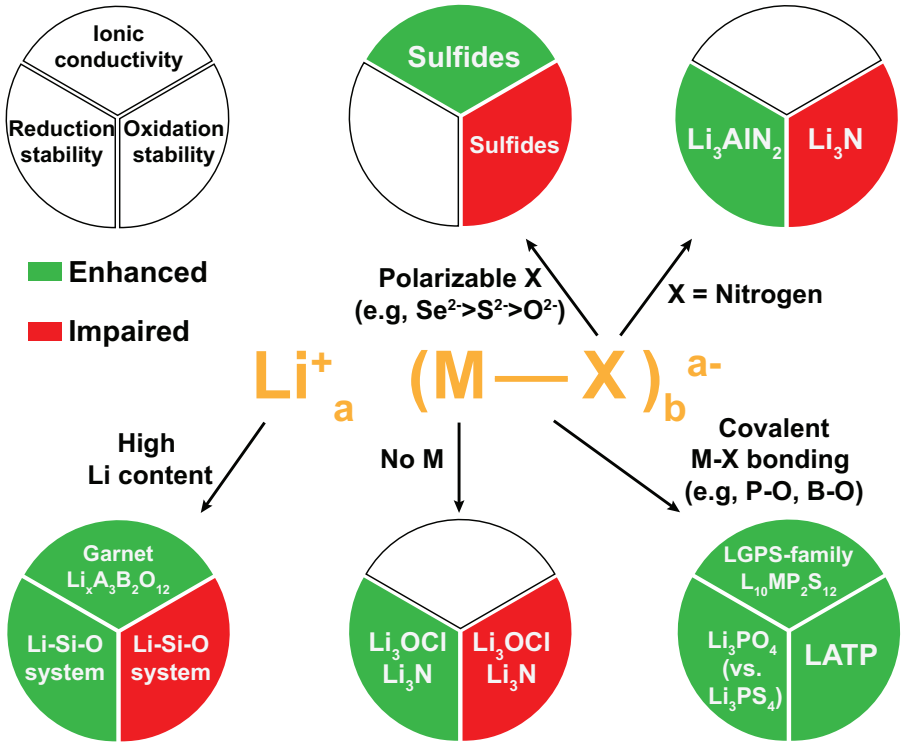

Figure 7: **Trade-offs between ionic conductivity and electrochemical stability upon tuning the SE composition.** M: non-lithium cation(s), X: anion. The pie chart represents the effect of the individual strategy on the ionic conductivity (upper sector), reduction stability (lower left sector), and oxidation stability (lower right sector) of the SE. The green regions indicate that the corresponding property is enhanced by the strategy, whereas the red regions indicate the inverse. The white regions indicate that the effect of the strategy is not clear. Examples illustrating each effect are provided in the corresponding sectors.

SEs has resulted in structural diversity that has greatly enlarged the parameter space for ionic conductivity optimization. Indeed, the best sulfide and oxide conductors such as LGPS, $Li_{9.54}Si_{1.74}P_{1.44}S_{11.7}Cl_{0.3}$, garnets, and NASICONs all contain at least one metal or metalloid element(s). However, these cations are often reduced against Li metal, creating an MCI at the SE/Li interface. To mitigate this issue, metal or metalloid cations that are more difficult to reduce (e.g., Ca^{2+}, La^{3+}) can be used, or the content of non-metal cations such as P^{5+} and H^{+} that can form a passivating SEI can be increased, as observed in the hydration of Na_3SbS_4[115]. Anion chemistry can also affect the reduction stability of metal cations, as reported by Zhu et al.[225,234] With the same cation, the reduction stability follows the trend: fluorides < sulfides < oxides < nitrides. Table 1 summarizes the anion-dependent stability of various cations against Li metal based on the computational and experimental data. The table also shows whether an SEI or MCI interphase is expected to form when the cation is reduced by Li metal. This table can serve as a reference for selecting dopants or designing the composition for new SEs and anode coatings. As noted by Zhu et al.[225], the nitrogen anion stabilizes numerous cations (e.g., Al^{3+}) against reduction by Li metal that would otherwise be reducible with other anion chemistries. However, these nitrides suffer from a low intrinsic oxidation limit typically below 2 V, making them difficult to pair with high-voltage cathodes[64,234].

Completely avoiding the use of reducible cations leads to absolute reduction stability against Li metal, which is the case for the nitride conductor Li_3N and antiperovskite conductors Li_3OCl and $Li_3OBr_{0.5}Cl_{0.5}$, as shown in Fig. 6. However, the lack of any covalent bonding with anions leads to an oxidation limit below 3 V for these materials. For antiperovskites, decomposition products such as LiCl and $LiClO_4$ may passivate the SE/cathode interface, as indicated by the measured wide voltage stability window[193]. For Li_3N, oxidation decomposition likely leads to

Table 1: **Types of interfaces between Li metal and SEs containing different cations based on computed Li–M–X phase diagrams (M: non-lithium cation, X: anion)** The computational classification is based on the Li–M–X phase diagram as an approximation[225]. If there is a M–X or Li–M–X compound that is stable against Li, the M cation is classified as "Stable against Li". If no such stable binary or ternary phase exists, the interphase is classified as an SEI–former (if the Li-stable phases are electron insulators) or an MCI–former (if otherwise). Note that the cations in parentheses have been experimentally confirmed, and only cations with elements in the first six periods in the periodic table are considered. Computational data from Zhu et al.[225,234] and the Materials Project[85].

Anion X	Stable against Li metal	SEI–formers	MCI–formers
O	Be^{2+}, Ca^{2+}, Sc^{3+}, Y^{3+}, Hf^{4+}, lanthanide series ($La^{3+,a,156,183}$)	H^{+}, N^{5+}, P^{5+}, S^{x+},Se^{x+}, Te^{x+}, Cl^{x+}, Br^{x+}, I^{x+} ($P^{5+,73}$)	Others ($Fe^{3+,157}$, $Zr^{4+,b,156}$, $Nb^{5+,156}$)
S	Ca^{2+}, Sr^{2+}, Ba^{2+}, lanthanide series[c]	Same as O chemistry ($H^{+,d,115}$, $P^{5+,52}$)	Others ($Ge^{4+,52,111}$, $Sn^{4+,112}$, $Si^{4+,112}$, $Sb^{4+,d,115}$)
Cl	K^{+}, Rb^{+}, Cs^{+}, Ca^{2+}, Sr^{2+}, Ba^{2+}, Yb^{2+}	Same as O chemistry	Others
Br	Na^{+}, K^{+}, Rb^{+}, Cs^{+}, Ca^{2+}, Sr^{2+}, Ba^{2+}, Yb^{2+}	Same as O chemistry	Others
N	Be^{2+}, Mg^{2+}, Ca^{2+}, Sr^{2+}, Sc^{3+}, Y^{3+}, Re^{3+}, B^{3+}, Al^{3+}, C^{4+}, Si^{4+},Ti^{4+}, Zr^{4+},Hf^{4+}, V^{5+}, Nb^{5+}, Ta^{5+}, Mn^{5+}, Cr^{6+}, Mo^{6+}, W^{6+}, lanthanide series	Same as O chemistry	Others

[a]In addition, Al^{3+} and Ta^{5+} are also observed to be stable against Li metal in experiments[156,156,199], although they are predicted to be reduced below 0.06 V for Al^{3+} in Li_5AlO_4 and 0.35 V for Ta^{5+} in Li_5TaO_5[85].

[b]Still in debate in experiments. Although the reduction of Zr^{4+} by Li metal was observed in XPS[100,155,156], apparent stability or passivation between Li metal and Zr^{4+}-containing SEs has been reported[150–152,156,206,207].

[c]Excluding Lu^{2+}, Tm^{2+}, Ho^{2+}, Dy^{2+} for the sulfide chemistry.

[d]Observed in Na SSBs.

continuous gas formation and SE consumption.

It has been shown that increasing the Li content shifts the electrochemical stability window down toward 0 V, as observed in the Li–Si–O system[66,67], directly leading to a trade-off between the oxidation and reduction stability. The decrease of oxidation stability with increasing Li content can be viewed as a result of the weakened covalency of the anions as they are increasingly interacting with Li. Increasing the Li content also typically benefits the ionic conductivity of an SE. This trend was observed in a statistical learning study of the ionic conductivity of crystalline SEs[235] and experimentally demonstrated in garnets[24] and the glass systems Li_2O–B_2O_3 and Li_2S–P_2S_5[236]. Hybridization, in contrast, can extend the stability window on both the oxidation and reduction limit by lowering the bonding state energy and elevating the anti-bonding state energy. The increase of the oxidation limit by hybridization was discussed above in the comparison between NASICON SEs and other oxide SEs. The hybridization effect on reduction limit can be demonstrated by comparing the reduction limit of Li_3PS_4 (1.69 V) with that of Li_3PO_4 (0.71 V). P–O bonding in Li_3PO_4 has a higher degree of hybridization than P-S bonding in Li_3PS_4, as indicated by their large bond energy difference (596.6 kJ/mol for P–O vs. 346 kJ/mol for P–S)[107].

7.2 Pitfalls of the electrochemical stability measurement using CV

Commercialized solid-state cells must provide consistent operation over thousands of cycles and excellent Coulombic efficiency, thereby requiring the minimization of interfacial reactions after an initial passivation, if any. Thus, extensive studies on the degradation behaviors and mechanisms at the electrode/SE interface are needed. In this context, it is important to note that CV, a conventional method that has been widely used to estimate the voltage stability of liquid electrolyte, can lead to an overestimated stability window of the SE if the data is

not interpreted carefully. Several stability windows determined from CV measurements are unphysically wide and have often been corrected by more careful follow-up studies. For instance, the claims of stability windows of 0–5 V for LGPS[32], 0–9 V for LLZO[26], and 0–8 V for Ba-doped Li_3OCl[193] defy basic chemistry. These oxidation limits are significantly higher than the thermodynamically predicted values and cannot be simply justified by the kinetic stabilization. As noted in several studies[50,100,234], the CV method only reliably detects the presence of either a non-passivating reaction forming an MCI that continues to grow (e.g., the reduction of LLT[180]), or a passivating decomposition reaction with a large enough reaction region. The absence of noticeable current at high voltages during a CV sweep is often taken as evidence of the wide voltage window of an SE when, in reality, a passivation layer could have formed or the reaction area may be restricted by the limited contact between the SE and planar electrode. When the reaction only forms a thin layer on the surface of the planar electrode, it may not be detectable under typical CV test conditions. For an oxidation reaction of Li_3PS_4 occurring over a 1-V window at a sweep rate of 0.1 mV s^{-1}, forming a 10-nm-thick layer on the planar electrode results in a calculated CV current of ~0.3 μA cm^{-2}, which is indeed on the same order of magnitude as those observed by Han et al. in the CV of a Li|LGPS|Pt cell[100] and by Swamy et al. for a Li|Li_3PS_4|C cell[104]. To capture the redox of the SE from such a small current, high-sensitivity CV measurements have indicated oxidation decomposition currents of a Na-ion conductor $Na_2(B_{12}H_{12})_{0.5}(B_{10}H_{10})_{0.5}$ on the nA cm^{-2} scale to begin at 3 V[237], which is significantly lower than the previous CV results[45,238]. Alternatively, mixing electronically conductive particles such as carbon with the SE to form a composite working electrode (WE) has been shown to increase the oxidation and reduction current by several orders of magnitude in the CV of a Li|SE|WE|semi-blocking electrode cell, giving rise to more visible oxidation and

reduction signals for voltage stability measurements[100,104,142].

Even with the use of a composite WE, choosing a cutoff current criterion for CV to determine the oxidation/reduction limit of the SE is difficult as the CV current strongly depends on the experimental setup and procedures[239]. Instead, these limits should be determined by the potential at which the oxidation/reduction current increases drastically during the sweeps. Dewald et al. additionally used the occurrence of the reduction peak of SE oxidation products to help determine the oxidation limits of several sulfide SEs[239]. In addition, a Li electrode has often been used as the counter and reference electrode for CV[26,32,240], but it may react with the SE and a true reference electrode is needed to accurately determine the applied potential on the working electrode[241]. These issues may be mitigated by using a three-electrode setup with a non-Li counter electrode (e.g., In[239,242], Au[103]) and a non-Li reference electrode (e.g., In[239,242], Ag_3SI/Ag mixture[103]). Because CV is an indirect method to characterize interfacial reactions, we believe it is good practice to supplement CV with other interface characterization techniques such as TEM and XPS[100,101,239] to confirm the voltage stability window and to capture detailed information on the reaction products.

In general, the use of high-sensitivity instruments, the magnification of the reaction signal (e.g., by increasing the reaction region, temperature or time), and the combination of various complementary characterization techniques are effective ways for characterizing interfacial reactions in experiments.

7.3 Performance metrics for SSBs

It is important to re-evaluate the commonly used performance metrics created for LIBs and consider their applicability in SSBs. In LIBs, the inventory management of Li ions is particularly important as the only lithium that cycles in the cell originates from the cathode. Therefore,

the Coulombic efficiency of LIBs must be very high[243,244], and the Li loss during the formation of the SEI layer should be minimized. Similarly for SSBs, ideally the cell would start "anode-less", where all the lithium starts in the cathode and plates and strips as Li metal at the anode. However, in typical lab solid-state cells, "extra" Li is available from a Li metal anode or from the breakdown of the Li-containing SE. For example, the oxidation decomposition of the SE can provide extra Li ions and electrons during charging. In some reports[95,104], oxidation decomposition products have provided extra reversible capacity over a few cycles. However, given that these capacities corresponds to conversion reactions, they are unlikely to contribute to stable long-term cycling; additionally, the conversion reaction may occur below the cathode cutoff voltage, thereby limiting the reversibility.

We note that decomposition reactions of the SE can contribute unknowingly to the temporary capacity of the battery, making it difficult to rely on Coulombic efficiency alone to gauge the stability of the SSB. For example, when discharged to a low voltage, the SE on the cathode side can be reduced and contribute to the discharge capacity, resulting in a Coulombic efficiency sometimes higher than 100%[69,94]. Therefore, one can in principle cycle the cell with a high Coulombic efficiency and limited capacity fade even when serious SE degradation occurs. At some point, the SE degradation will, however, increase the impedance to the point where the capacity loss occurs at the imposed current rates outweighs the capacity contribution from the SE decomposition. It is worthwhile to mention that energy efficiency is being increasingly used as a metric for LIBs[245,246]. Besides incorporating Coulombic efficiency, energy efficiency also captures the voltage losses in discharge due to the impedance growth.

Hence, it is critical to directly measure the cell impedance and the rate of its growth. Furthermore, these measurements are particularly important at high temperatures and high

state-of-charge; thus, a calendar-life test should be performed during which the impedance growth is monitored over long-term storage of the charged battery, and the discharge capacity should be measured before and after the calendar-life testing. Such tests can reveal the effect of even minor interfacial reactions on the impedance growth and cell performance. In addition, to achieve high energy density in SSBs, high cathode and low SE loading within the cathode composite is required, making the negative effect of SE decomposition on the cell performance even more pronounced.

8 Conclusions and perspectives

The mechanisms by which Li-ion conductors derive their high ionic conductivity have become reasonably well established. Polarizable anions such as S^{2-} can shield the electrostatic interactions between the host structure and the migrating Li ions[49]. The topology of the host structure can be optimized to keep the coordination of Li as constant as possible[247]. In addition, a high Li content can create frustrated Li arrangements and force Li to reside in high-energy sites, from which migration is easier[248,249]. These understandings have led to the rapid development of new superionic conductors. The next foremost task in SSB development is the reduction of the high interfacial reactivity and resistance. Commercial SSBs will require a high loading density of active material with a low SE content in the cathode composite and a thin separator, which will require careful management of the reactivity of the SE to minimize the increase in resistivity along the Li-ion transport path. Based on the experimental and theoretical results to date, it appears unlikely that any SE materials in use today are absolutely stable against high-voltage cathodes as well as Li metal, thereby requiring either the use of stable coatings or the formation of stable passivation layers. Hence, characterizing the passivation interphases between SEs and

electrodes and their growth should be prioritized for the SSB field. Even though it may be possible to develop conductors that are thermodynamically stable against both Li metal and high-voltage cathodes, many of the factors that enhance Li-ion conductivity (more polarizable anions, high Li content, reducible cations) narrow the electrochemical stability window.

The recent advances in modeling and characterization of interfaces in SSBs have greatly narrowed the gap between experimental observations and computational predictions. For example, the low calculated oxidation stability limits for sulfides (< 2.5 V) and oxides (< 5 V) based on thermodynamic models contrasted sharply with early claims of > 5-V stability for many SEs. More careful CV and direct characterizations in recent studies have resolved these discrepancies and validated the computational results[95,100]. High-throughput computing[250,251] and the establishment of large databases of *ab initio* phase diagrams, such as the Materials Project[84], have made it fairly straightforward to compute the thermodynamic reaction products that will form at an interface[85]. Many of these predicted decomposition products have been confirmed using advanced characterization techniques including XPS, Raman spectroscopy, XRD, TEM/STEM, EDS, EELS, and TOF-SIMS. Even when the precisely predicted interphases are not observed in experiments, the computational results often capture the qualitative features of the interfacial reactions, such as the redox center driving the electrochemical decomposition, the preferred bond formation upon chemical mixing, and the formation of a stable interface, an MCI, or an SEI. The predictive power of these interface models can effectively guide the reverse engineering of interfaces in SSBs, as recently demonstrated in the stabilization of the Na_3SbS_4/Na interface by hydration[115].

Nevertheless, factors such as the rate of elemental diffusion, new phase nucleation, and whether new phases formed at the interface will be amorphous or crystalline are much more

difficult to predict using current computational methods. The time scale relevant to experimental observations cannot be achieved in explicit interface modeling using *ab initio* techniques. Further development of these models should aim to include the kinetic factors to predict, for example, the most likely reaction pathways and products (including amorphous phases), stricter bounds for kinetic stabilization, and the upper bound of the processing temperature. On the experimental side, efforts should be made to elucidate the composition and structure of individual interfaces and interphases under processing and battery cycling conditions and how they individually affect the cell performance. Stable interfaces should be distinguished from those at which passivation slows down the reaction. This task requires the development of non-destructive spatially resolved characterization techniques, as well as *in situ* or *operando* techniques that can reveal the compositional and structural evolution of the interface. Such experimental data can be used synergistically with computational modeling to shed light on the mechanisms and kinetic pathways of interfacial reactions.

9 Acknowledgements

This work on ionic conductivity design was funded by the Samsung Advanced Institute of Technology. The development of the interfacial reactivity theory was funded by the Materials Project Program (Grant No. KC23MP) through the U.S. Department of Energy, Office of Science, Office of Basic Energy Sciences, Materials Sciences and Engineering Division under Contract No. DE-AC02-05CH11231. Some of the work on sulfide electrolytes was supported by the Assistant Secretary for Energy Efficiency and Renewable Energy, Vehicle Technologies Office of the U.S. Department of Energy under Contract No. DE-AC02-05CH11231 under the Advanced Battery Materials Research (BMR) Program.

10 Author contributions

G.C. conceived the manuscript. Y.X. researched the data. S.B. and Y.X. wrote the section on sulfides. Y.X. wrote the sections on garnets and coatings. J.C.K. wrote the sections on LiPON and antiperovskites. Y.W. and Y.X. wrote the sections on perovskites and NASICONs. G.C., Y.X. and L.J.M. wrote the sections on discussion and conclusions. Y.X., Y.W. and L.J.M. designed the table and figures. All authors edited and reviewed the manuscript before submission.

11 Competing interests statement

The authors declare no competing interests.

References

1. P. Arora, R. E. White, & M. Doyle. Capacity fade mechanisms and side reactions in lithium-ion batteries. *J. Electrochem. Soc.*, **145**, 3647–3667 (1998).
2. J. Vetter, P. Novák, M. R. Wagner, C. Veit, K. C. Möller, J. O. Besenhard, M. Winter, M. Wohlfahrt-Mehrens, C. Vogler, & A. Hammouche. Ageing mechanisms in lithium-ion batteries. *J. Power Sources*, **147**, 269–281 (2005).
3. J. Li, C. Ma, M. Chi, C. Liang, & N. J. Dudney. Solid electrolyte: the key for high-voltage lithium batteries. *Adv. Energy Mater.*, **5**, 1401408 (2015).
4. W. Xu, J. Wang, F. Ding, X. Chen, E. Nasybulin, Y. Zhang, & J.-G. Zhang. Lithium metal anodes for rechargeable batteries. *Energy Environ. Sci.*, **7**, 513–537 (2014).
5. D. Lin, Y. Liu, & Y. Cui. Reviving the lithium metal anode for high-energy batteries. *Nat. Publ. Gr.*, **12**, 194–206 (2017).
6. I. Epelboin, M. Froment, M. Garreau, J. Thevenin, & D. Warin. Behavior of secondary lithium and aluminum-lithium electrodes in propylene carbonate. *J. Electrochem. Soc.*, **127**, 2100–2104 (1980).
7. R. Bhattacharyya, B. Key, H. Chen, A. S. Best, A. F. Hollenkamp, & C. P. Grey. In situ NMR observation of the formation of metallic lithium microstructures in lithium batteries. *Nat. Mater.*, **9**, 504–510 (2010).
8. X. Yu, J. Bates, G. Jellison, & F. Hart. A stable thin-film lithium electrolyte: lithium phosphorus oxynitride. *J. Electrochem. Soc.*, **144**, 524–532 (1997).
9. F. Han, J. Yue, X. Zhu, & C. Wang. Suppressing Li dendrite formation in Li_2S–P_2S_5 solid electrolyte by LiI incorporation. *Adv. Energy Mater.*, **8**, 1703644 (2018).
10. L. Porz, T. Swamy, B. W. Sheldon, D. Rettenwander, T. Frömling, H. L. Thaman, S. Berendts, R. Uecker, W. C. Carter, & Y.-M. Chiang. Mechanism of lithium metal penetration through inorganic solid electrolytes. *Adv. Energy Mater.*, **7**, 1701003 (2017).
11. Y. Ren, Y. Shen, Y. Lin, & C.-W. Nan. Direct observation of lithium dendrites inside garnet-type lithium-ion solid electrolyte. *Electrochem. Commun.*, **57**, 27–30 (2015).

12. L. O. Valøen & J. N. Reimers. Transport properties of $LiPF_6$-based Li-ion battery electrolytes. *J. Electrochem. Soc.*, **152**, A882–A891 (2005).

13. A. Ponrouch, E. Marchante, M. Courty, J.-M. Tarascon, & M. R. Palacín. In search of an optimized electrolyte for Na-ion batteries. *Energy Environ. Sci.*, **5**, 8572–8583 (2012).

14. J. Goodenough, H.-P. Hong, & J. Kafalas. Fast Na^+-ion transport in skeleton structures. *Mater. Res. Bull.*, **11**, 203–220 (1976).

15. U. Von Alpen, M. F. Bell, & H. H. Höfer. Compositional dependence of the electrochemical and structural parameters in the Nasicon system ($Na_{1+x}Si_xZr_2P_{3-x}O_{12}$). *Solid State Ionics*, **3**, 215–218 (1981).

16. M. Subramanian, R. Subramanian, & A. Clearfield. Lithium ion conductors in the system $AB(IV)_2(PO_4)_3$ (B = Ti, Zr and Hf). *Solid State Ionics*, **18**, 562–569 (1986).

17. H. Aono, E. Sugimoto, Y. Sadaoka, N. Imanaka, & G.-y. Adachi. Ionic conductivity of solid electrolytes based on lithium titanium phosphate. *J. Electrochem. Soc.*, **137**, 1023–1027 (1990).

18. H. Khireddine, P. Fabry, A. Caneiro, & B. Bochu. Optimization of NASICON composition for Na^+ recognition. *Sensors Actuators B Chem.*, **40**, 223–230 (1997).

19. J. W. Fergus. Ion transport in sodium ion conducting solid electrolytes. *Solid State Ionics*, **227**, 102–112 (2012).

20. J. Briant & G. Farrington. Ionic conductivity in lithium and lithium sodium beta alumina. *J. Electrochem. Soc.*, **128**, 1830–1834 (1981).

21. Y.-f. Yu Yao & J. T. Kummer. Ion exchange properties of and rates of ionic diffusion in beta-alumina. *J. Inorg. Nucl. Chem.*, **29**, 2453–2475 (1967).

22. M. S. Whittingham & R. A. Huggins. Measurement of sodium ion transport in beta alumina using reversible solid electrodes. *J. Chem. Phys.*, **54**, 414–416 (1971).

23. X. Lu, J. P. Lemmon, V. Sprenkle, & Z. Yang. Sodium-beta alumina batteries: status and challenges. *Jom*, **62**, 31–36 (2010).

24. V. Thangadurai, S. Narayanan, & D. Pinzaru. Garnet-type solid-state fast Li ion conductors for Li batteries: critical review. *Chem. Soc. Rev.*, **43**, 4714–27 (2014).

25. R. Murugan, V. Thangadurai, & W. Weppner. Fast lithium ion conduction in garnet-type $Li_7La_3Zr_2O_{12}$. *Angew. Chem. Int. Ed.*, **46**, 7778–7781 (2007).

26. S. Ohta, T. Kobayashi, & T. Asaoka. High lithium ionic conductivity in the garnet-type oxide $Li_{7-X}La_3(Zr_{2-X}, Nb_X)O_{12}$ (X=0–2). *J. Power Sources*, **196**, 3342–3345 (2011).

27. J. Allen, J. Wolfenstine, E. Rangasamy, & J. Sakamoto. Effect of substitution (Ta, Al, Ga) on the conductivity of $Li_7La_3Zr_2O_{12}$. *J. Power Sources*, **206**, 315–319 (2012).

28. S. Stramare, V. Thangadurai, & W. Weppner. Lithium lanthanum titanates: a review. *Chem. Mater.*, **15**, 3974–3990 (2003).

29. Y. Zhao & L. Daemen. Superionic conductivity in lithium-rich anti-perovskites. *J. Am. Chem. Soc.*, **134**, 15042–15047 (2012).

30. R. Kanno & M. Murayama. Lithium ionic conductor thio-LISICON: the Li_2S–GeS_2–P_2S_5 system. *J. Electrochem. Soc.*, **148**, A742–A746 (2001).

31. M. Murayama, N. Sonoyama, A. Yamada, & R. Kanno. Material design of new lithium ionic conductor, thio-LISICON, in the Li_2S–P_2S_5 system. *Solid State Ionics*, **170**, 173–180 (2004).

32. N. Kamaya, K. Homma, Y. Yamakawa, M. Hirayama, R. Kanno, M. Yonemura, T. Kamiyama, Y. Kato, S. Hama, K. Kawamoto, & A. Mitsui. A lithium superionic conductor. *Nat. Mater.*, **10**, 682–686 (2011).

33. Y. Kato, S. Hori, T. Saito, K. Suzuki, M. Hirayama, A. Mitsui, M. Yonemura, H. Iba, & R. Kanno. High-power all-solid-state batteries using sulfide superionic conductors. *Nat. Energy*, **1**, 16030 (2016).

34. S. P. Ong, Y. Mo, W. D. Richards, L. Miara, H. S. Lee, & G. Ceder. Phase stability, electrochemical stability and ionic conductivity of the $Li_{10\pm1}MP_2X_{12}$ (M = Ge, Si, Sn, Al or P, and X = O, S or Se) family of superionic conductors. *Energy Environ. Sci.*, **6**, 148–156 (2013).

35. A. Hayashi, S. Hama, H. Morimoto, M. Tatsumisago, & T. Minami. Preparation of Li_2S–P_2S_5 amorphous solid electrolytes by mechanical milling. *J. Am. Ceram. Soc.*, **84**, 477–479 (2001).

36. Y. Seino, T. Ota, K. Takada, A. Hayashi, & M. Tatsumisago. A sulphide lithium super ion conductor is superior to liquid ion conductors for use in rechargeable batteries. *Energy Environ. Sci.*, **7**, 627–631 (2014).

37. H.-J. Deiseroth, S.-T. Kong, H. Eckert, J. Vannahme, C. Reiner, T. Zaiß, & M. Schlosser. Li_6PS_5X: a class of crystalline Li-rich solids with an unusually high Li^+ mobility. *Angew. Chemie Int. Ed.*, **47**, 755–758 (2008).

38. R. P. Rao & S. Adams. Studies of lithium argyrodite solid electrolytes for all-solid-state batteries. *Phys. Status Solidi A*, **208**, 1804–1807 (2011).

39. M. Jansen & U. Henseler. Synthesis, structure determination, and ionic conductivity of sodium tetrathiophosphate. *J. Solid State Chem.*, **99**, 110–119 (1992).

40. A. Hayashi, K. Noi, A. Sakuda, & M. Tatsumisago. Superionic glass-ceramic electrolytes for room-temperature rechargeable sodium batteries. *Nat. Commun.*, **3**, 856 (2012).

41. S. H. Bo, Y. Wang, J. C. Kim, W. D. Richards, & G. Ceder. Computational and experimental investigations of Na-ion conduction in cubic Na_3PSe_4. *Chem. Mater.*, **28**, 252–258 (2016).

42. A. Banerjee, K. H. Park, J. W. Heo, Y. J. Nam, C. K. Moon, S. M. Oh, S.-T. Hong, & Y. S. Jung. Na_3SbS_4: a solution processable sodium superionic conductor for all-solid-state sodium-ion batteries. *Angew. Chem. Int. Ed.*, **128**, 9786–9790 (2016).

43. W. D. Richards, T. Tsujimura, L. J. Miara, Y. Wang, J. C. Kim, S. P. Ong, I. Uechi, N. Suzuki, & G. Ceder. Design and synthesis of the superionic conductor $Na_{10}SnP_2S_{12}$. *Nat. Commun.*, **7**, 11009 (2016).

44. Z. Zhang, E. Ramos, F. Lalère, A. Assoud, K. Kaup, P. Hartman, & L. F. Nazar. $Na_{11}Sn_2PS_{12}$: a new solid state sodium superionic conductor. *Energy Environ. Sci.*, **11**, 87–93 (2018).

45. T. J. Udovic, M. Matsuo, W. S. Tang, H. Wu, V. Stavila, A. V. Soloninin, R. V. Skoryunov, O. A. Babanova, A. V. Skripov, J. J. Rush, A. Unemoto, H. Takamura, & S. I. Orimo. Exceptional superionic conductivity in disordered sodium decahydro-closo-decaborate. *Adv. Mater.*, **26**, 7622–7626 (2014).

46. W. S. Tang, M. Matsuo, H. Wu, V. Stavila, W. Zhou, A. A. Talin, A. V. Soloninin, R. V. Skoryunov, O. A. Babanova, A. V. Skripov, et al. Liquid-like ionic conduction in solid lithium and sodium monocarba-closo-decaborates near or at room temperature. *Adv. Energy Mater.*, **6**, 1502237 (2016).

47. A. Sakuda, A. Hayashi, & M. Tatsumisago. Interfacial observation between $LiCoO_2$ electrode and Li_2S–P_2S_5 solid electrolytes of all-solid-state lithium secondary batteries using transmission electron microscopy. *Chem. Mater.*, **22**, 949–956 (2010).

48. K. Takada, N. Ohta, L. Zhang, X. Xu, B. T. Hang, T. Ohnishi, M. Osada, & T. Sasaki. Interfacial phenomena in solid-state lithium battery with sulfide solid electrolyte. *Solid State Ionics*, **225**, 594–597 (2012).

49. K. Takada. Progress and prospective of solid-state lithium batteries. *Acta Mater.*, **61**, 759–770 (2013).

50. Y. Tian, T. Shi, W. D. Richards, J. Li, J. C. Kim, S. Bo, & G. Ceder. Compatibility issues between electrodes and electrolytes in solid-state batteries. *Energy Environ. Sci.*, **10**, 1150–1166 (2017).

51. J. M. Whiteley, J. H. Woo, E. Hu, K.-W. Nam, & S.-H. Lee. Empowering the lithium metal battery through a silicon-based superionic conductor. *J. Electrochem. Soc.*, **161**, A1812–A1817 (2014).

52. S. Wenzel, S. Randau, T. Leichtweiß, D. A. Weber, J. Sann, W. G. Zeier, & J. Janek. Direct observation of the interfacial instability of the fast ionic conductor $Li_{10}GeP_2S_{12}$ at the lithium metal anode. *Chem. Mater.*, **28**, 2400–2407 (2016).

53. K. Hoshina, K. Dokko, & K. Kanamura. Investigation on electrochemical interface between $Li_4Ti_5O_{12}$ and $Li_{1+x}Al_xTi_{2-x}(PO_4)_3$ NASICON-type solid electrolyte. *J. Electrochem. Soc.*, **152**, A2138–A2142 (2005).

54. M. Tatsumisago, M. Nagao, & A. Hayashi. Recent development of sulfide solid electrolytes and interfacial modification for all-solid-state rechargeable lithium batteries. *J. Asian Ceram. Soc.*, **1**, 17–25 (2013).

55. S. Ohta, J. Seki, Y. Yagi, Y. Kihira, T. Tani, & T. Asaoka. Co-sinterable lithium garnet-type oxide electrolyte with cathode for all-solid-state lithium ion battery. *J. Power Sources*, **265**, 40–44 (2014).

56. N. Ohta, K. Takada, L. Zhang, R. Ma, M. Osada, & T. Sasaki. Enhancement of the high-rate capability of solid-state lithium batteries by nanoscale interfacial modification. *Adv. Mater.*, **18**, 2226–2229 (2006).

57. N. Ohta, K. Takada, I. Sakaguchi, L. Zhang, R. Ma, K. Fukuda, M. Osada, & T. Sasaki. $LiNbO_3$-coated $LiCoO_2$ as cathode material for all solid-state lithium secondary batteries. *Electrochem. Commun.*, **9**, 1486–1490 (2007).

58. K. Takada, N. Ohta, L. Zhang, K. Fukuda, I. Sakaguchi, R. Ma, M. Osada, & T. Sasaki. Interfacial modification for high-power solid-state lithium batteries. *Solid State Ionics*, **179**, 1333–1337 (2008).

59. E. J. Cheng, A. Sharafi, & J. Sakamoto. Intergranular Li metal propagation through polycrystalline $Li_{6.25}Al_{0.25}La_3Zr_2O_{12}$ ceramic electrolyte. *Electrochim. Acta*, **223**, 85–91 (2017).

60. R. Koerver, I. Aygn, T. Leichtweiß, C. Dietrich, W. Zhang, J. O. Binder, P. Hartmann, W. G. Zeier, & J. Janek. Capacity fade in solid-state batteries: interphase formation and chemomechanical processes in nickel-rich layered oxide cathodes and lithium thiophosphate solid electrolytes. *Chem. Mater.*, **29**, 5574–5582 (2017).

61. L. Cheng, E. J. Crumlin, W. Chen, R. Qiao, H. Hou, S. F. Lux, V. Zorba, R. Russo, R. Kostecki, Z. Liu, et al. The origin of high electrolyte–electrode interfacial resistances in lithium cells containing garnet type solid electrolytes. *Phys. Chem. Chem. Phys.*, **16**, 18294–18300 (2014).

62. X. Han, Y. Gong, K. K. Fu, X. He, G. T. Hitz, J. Dai, A. Pearse, B. Liu, H. Wang, G. Rubloff, et al. Negating interfacial impedance in garnet-based solid-state Li metal batteries. *Nat. Mater.*, **16**, 572–579 (2017).

63. S. Wenzel, T. Leichtweiss, D. Krüger, J. Sann, & J. Janek. Interphase formation on lithium solid electrolytes - an in situ approach to study interfacial reactions by photoelectron spectroscopy. *Solid State Ionics*, **278**, 98–105 (2015).

64. W. D. Richards, L. J. Miara, Y. Wang, J. C. Kim, & G. Ceder. Interface stability in solid-state batteries. *Chem. Mater.*, **28**, 266–273 (2016).

65. Y. Zhu, X. He, & Y. Mo. Origin of outstanding stability in the lithium solid electrolyte materials: insights from thermodynamic analyses based on first-principles calculations. *ACS Appl. Mater. Interfaces*, **7**, 23685–23693 (2015).

66. Y. Zhu, X. He, & Y. Mo. First principles study on electrochemical and chemical stability of solid electrolyte–electrode interfaces in all-solid-state Li-ion batteries. *J. Mater. Chem. A*, **4**, 3253–3266 (2016).

67. Y. Xiao, L. J. Miara, Y. Wang, & G. Ceder. Computational screening of cathode coatings for solid-state batteries. *Joule*, **3**, 1252–1275 (2019).

68. W. Zhang, T. Leichtweiß, S. P. Culver, R. Koerver, D. Das, D. A. Weber, W. G. Zeier, & J. Janek. The detrimental effects of carbon additives in $Li_{10}GeP_2S_{12}$-based solid-state batteries. *ACS Appl. Mater. Interfaces*, **9**, 35888–35896 (2017).

69. K. Yoon, J.-J. Kim, W. M. Seong, M. H. Lee, & K. Kang. Investigation on the interface between $Li_{10}GeP_2S_{12}$ electrolyte and carbon conductive agents in all-solid-state lithium battery. *Sci. Rep.*, **8**, 8066 (2018).

70. R. Koerver, F. Walther, I. Aygün, J. Sann, C. Dietrich, W. G. Zeier, & J. Janek. Redox-active cathode interphases in solid-state batteries. *J. Mater. Chem. A*, **5**, 22750–22760 (2017).

71. L. Xu, S. Tang, Y. Cheng, K. Wang, J. Liang, C. Liu, Y.-C. Cao, F. Wei, & L. Mai. Interfaces in solid-state lithium batteries. *Joule*, **2**, 1991–2015 (2018).

72. A. Brazier, L. Dupont, L. Dantras-Laffont, N. Kuwata, J. Kawamura, & J.-M. Tarascon. First cross-section observation of an all solid-state lithium-ion "nanobattery" by transmission electron microscopy. *Chem. Mater.*, **20**, 2352–2359 (2008).

73. A. Schwöbel, R. Hausbrand, & W. Jaegermann. Interface reactions between LiPON and lithium studied by in-situ X-ray photoemission. *Solid State Ionics*, **273**, 51–54 (2015).

74. A. Sharafi, E. Kazyak, A. L. Davis, S. Yu, T. Thompson, D. J. Siegel, N. P. Dasgupta, & J. Sakamoto. Surface chemistry mechanism of ultra-low interfacial resistance in the solid-state electrolyte $Li_7La_3Zr_2O_{12}$. *Chem. Mater.*, **29**, 7961–7968 (2017).

75. M. K. Aydinol, A. F. Kohan, G. Ceder, K. Cho, & J. Joannopoulos. Ab initio study of lithium intercalation in metal oxides and metal dichalcogenides. *Phys. Rev. B*, **56**, 1354–1365 (1997).

76. F. Wang, R. Robert, N. A. Chernova, N. Pereira, F. Omenya, F. Badway, X. Hua, M. Ruotolo, R. Zhang, L. Wu, et al. Conversion reaction mechanisms in lithium ion batteries: study of the binary metal fluoride electrodes. *J. Am. Chem. Soc.*, **133**, 18828–18836 (2011).

77. F. Klein, B. Jache, A. Bhide, & P. Adelhelm. Conversion reactions for sodium-ion batteries. *Phys. Chem. Chem. Phys.*, **15**, 15876–15887 (2013).

78. A. Urban, D.-H. Seo, & G. Ceder. Computational understanding of Li-ion batteries. *npj Comput. Mater.*, **2**, 16002 (2016).

79. H. Visbal, Y. Aihara, S. Ito, T. Watanabe, Y. Park, & S. Doo. The effect of diamond-like carbon coating on $LiNi_{0.8}Co_{0.15}Al_{0.05}O_2$ particles for all solid-state lithium-ion batteries based on Li_2S–P_2S_5 glass-ceramics. *J. Power Sources*, **314**, 85–92 (2016).

80. K. H. Kim, Y. Iriyama, K. Yamamoto, S. Kumazaki, T. Asaka, K. Tanabe, C. A.J. Fisher, T. Hirayama, R. Murugan, & Z. Ogumi. Characterization of the interface between $LiCoO_2$ and $Li_7La_3Zr_2O_{12}$ in an all-solid-state rechargeable lithium battery. *J. Power Sources*, **196**, 764–767 (2011).

81. M. Zarabian, M. Bartolini, P. Pereira-Almao, & V. Thangadurai. X-ray photoelectron spectroscopy and AC impedance spectroscopy studies of Li-La-Zr-O solid electrolyte thin film/$LiCoO_2$ cathode interface for all-solid-state Li batteries. *J. Electrochem. Soc.*, **164**, A1133–A1139 (2017).

82. L. Miara, A. Windmüller, C. L. Tsai, W. D. Richards, Q. Ma, S. Uhlenbruck, O. Guillon, & G. Ceder. About the compatibility between high voltage spinel cathode materials and solid oxide electrolytes as a function of temperature. *ACS Appl. Mater. Interfaces*, **8**, 26842–26850 (2016).

83. A. T. Appapillai, A. N. Mansour, J. Cho, & Y. Shao-Horn. Microstructure of $LiCoO_2$ with and without "$AlPO_4$" nanoparticle coating: combined STEM and XPS studies. *Chem. Mater.*, **19**, 5748–5757 (2007).

84. A. Jain, S. P. Ong, G. Hautier, W. Chen, W. D. Richards, S. Dacek, S. Cholia, D. Gunter, D. Skinner, G. Ceder, & K. A. Persson. Commentary: The Materials Project: a materials genome approach to accelerating materials innovation. *APL Mater.*, **1**, 011002 (2013).

85. Materials Project. `http://www.materialsproject.org`.

86. N. D. Lepley & N. A. W. Holzwarth. Modeling interfaces between solids: application to Li battery materials. *Phys. Rev. B*, **92**, 1–15 (2015).

87. J. Haruyama, K. Sodeyama, & Y. Tateyama. Cation mixing properties toward Co diffusion at the $LiCoO_2$ cathode/sulfide electrolyte interface in a solid-state battery. *ACS Appl. Mater. Interfaces*, **9**, 286–292 (2016).

88. Z.-M. Xu, S.-H. Bo, & H. Zhu. $LiCrS_2$ and $LiMnS_2$ cathodes with extraordinary mixed electron–ion conductivities and favorable interfacial compatibilities with sulfide electrolyte. *ACS Appl. Mater. Interfaces*, **10**, 36941–36953 (2018).

89. S. Sicolo, M. Fingerle, R. Hausbrand, & K. Albe. Interfacial instability of amorphous LiPON against lithium: a combined density functional theory and spectroscopic study. *J. Power Sources*, **354**, 124–133 (2017).

90. M. Sumita, Y. Tanaka, M. Ikeda, & T. Ohno. Charged and discharged states of cathode/sulfide electrolyte interfaces in all-solid-state lithium ion batteries. *J. Phys. Chem. C*, **120**, 13332–13339 (2016).

91. L. E. Camacho-Forero & P. B. Balbuena. Exploring interfacial stability of solid-state electrolytes at the lithium-metal anode surface. *J. Power Sources*, **396**, 782–790 (2018).

92. H. Tang, Z. Deng, Z. Lin, Z. Wang, I.-H. Chu, C. Chen, Z. Zhu, C. Zheng, & S. P. Ong. Probing solid–solid interfacial reactions in all-solid-state sodium-ion batteries with first-principles calculations. *Chem. Mater.*, **30**, 163–173 (2017).

93. Z. Liu, W. Fu, E. A. Payzant, X. Yu, Z. Wu, N. J. Dudney, J. Kiggans, K. Hong, A. J. Rondinone, & C. Liang. Anomalous high ionic conductivity of nanoporous β-Li_3PS_4. *J. Am. Chem. Soc.*, **135**, 975–978 (2013).

94. F. Han, T. Gao, Y. Zhu, K. J. Gaskell, & C. Wang. A battery made from a single material. *Adv. Mater.*, **27**, 3473–3483 (2015).

95. T. Hakari, M. Deguchi, K. Mitsuhara, T. Ohta, K. Saito, Y. Orikasa, Y. Uchimoto, Y. Kowada, A. Hayashi, & M. Tatsumisago. Structural and electronic-state changes of a sulfide solid electrolyte during the Li deinsertion–insertion processes. *Chem. Mater.*, **29**, 4768–4774 (2017).

96. A. Hayashi, H. Muramatsu, T. Ohtomo, S. Hama, & M. Tatsumisago. Improvement of chemical stability of Li_3PS_4 glass electrolytes by adding M_xO_y (M = Fe, Zn, and Bi) nanoparticles. *J. Mater. Chem. A*, **1**, 6320–6326 (2013).

97. G. Oh, M. Hirayama, O. Kwon, K. Suzuki, & R. Kanno. Bulk-type all solid-state batteries with 5 V class $LiNi_{0.5}Mn_{1.5}O_4$ cathode and $Li_{10}GeP_2S_{12}$ solid electrolyte. *Chem. Mater.*, **28**, 2634–2640 (2016).

98. Y. Mo, S. P. Ong, & G. Ceder. First principles study of the $Li_{10}GeP_2S_{12}$ lithium super ionic conductor material. *Chem. Mater.*, **24**, 15–17 (2012).

99. I.-H. Chu, H. Nguyen, S. Hy, Y.-C. Lin, Z. Wang, Z. Xu, Z. Deng, Y. S. Meng, & S. P. Ong. Insights into the performance limits of the $Li_7P_3S_{11}$ superionic conductor: a combined first-principles and experimental study. *ACS Appl. Mater. Interfaces*, **8**, 7843–7853 (2016).

100. F. Han, Y. Zhu, X. He, Y. Mo, & C. Wang. Electrochemical stability of $Li_{10}GeP_2S_{12}$ and $Li_7La_3Zr_2O_{12}$ solid electrolytes. *Adv. Energy Mater.*, **6**, 1–9 (2016).

101. X. Wu, C. Villevieille, P. Novák, & M. El Kazzi. Monitoring the chemical and electronic properties of electrolyte–electrode interfaces in all-solid-state batteries using operando x-ray photoelectron spectroscopy. *Phys. Chem. Chem. Phys.*, **20**, 11123–11129 (2018).

102. P. Bron, S. Johansson, K. Zick, J. Schmedt auf der Günne, S. Dehnen, & B. Roling. $Li_{10}SnP_2S_{12}$: an affordable lithium superionic conductor. *J. Am. Chem. Soc.*, **135**, 15694–15697 (2013).

103. I. Tarhouchi, V. Viallet, P. Vinatier, & M. Ménétrier. Electrochemical characterization of $Li_{10}SnP_2S_{12}$: an electrolyte or a negative electrode for solid state Li-ion batteries? *Solid State Ionics*, **296**, 18–25 (2016).

104. T. Swamy, X. Chen, & Y.-M. Chiang. Electrochemical redox behavior of Li-ion conducting sulfide solid electrolytes. *Chem. Mater.*, **31**, 707–713 (2019).

105. W. Zhang, F. Richter, S. P. Culver, T. Leichtweiß, J. G. Lozano, C. Dietrich, P. G. Bruce, W. G. Zeier, & J. Janek. Degradation mechanisms at the $Li_{10}GeP_2S_{12}/LiCoO_2$ cathode interface in an all-solid-state lithium ion battery. *ACS Appl. Mater. Interfaces*, **10**, 22226–22236 (2018).

106. V. Lacivita, Y. Wang, S.-H. Bo, & G. Ceder. Ab initio investigation of the stability of electrolyte/electrode interfaces in all-solid-state Na batteries. *J. Mater. Chem. A*, **7**, 8144–8155 (2019).

107. J. A. Dean. *Lange's handbook of chemistry*. New York; London: McGraw-Hill, Inc., (1999).

108. H. Tsukasaki, T. Uchiyama, K. Yamamoto, S. Mori, Y. Uchimoto, H. Kowada, A. Hayashi, & M. Tatsumisago. Exothermal mechanisms in the charged $LiNi_{1/3}Mn_{1/3}Co_{1/3}O_2$ electrode layers for sulfide-based all-solid-state lithium batteries. *J. Power Sources*, **434**, 226714 (2019).

109. L. Sang, R. T. Haasch, A. A. Gewirth, & R. G. Nuzzo. Evolution at the solid electrolyte/gold electrode interface during lithium deposition and stripping. *Chem. Mater.*, **29**, 3029–3037 (2017).

110. S. Wenzel, D. A. Weber, T. Leichtweiss, M. R. Busche, J. Sann, & J. Janek. Interphase formation and degradation of charge transfer kinetics between a lithium metal anode and highly crystalline $Li_7P_3S_{11}$ solid electrolyte. *Solid State Ionics*, **286**, 24–33 (2016).

111. S.-J. Choi, S.-H. Lee, Y.-C. Ha, J.-H. Yu, C.-H. Doh, Y. Lee, J.-W. Park, S.-M. Lee, & H.-C. Shin. Synthesis and electrochemical characterization of a glass-ceramic $Li_7P_2S_8I$ solid electrolyte for all-solid-state Li-ion batteries. *J. Electrochem. Soc.*, **165**, A957–A962 (2018).

112. P. Bron, B. Roling, & S. Dehnen. Impedance characterization reveals mixed conducting interphases between sulfidic superionic conductors and lithium metal electrodes. *J. Power Sources*, **352**, 127–134 (2017).

113. M. Suyama, A. Kato, A. Sakuda, A. Hayashi, & M. Tatsumisago. Lithium dissolution/deposition behavior with Li_3PS_4-LiI electrolyte for all-solid-state batteries operating at high temperatures. *Electrochim. Acta*, **286**, 158–162 (2018).

114. E. A. Wu, C. S. Kompella, Z. Zhu, J. Z. Lee, S. C. Lee, I.-H. Chu, H. Nguyen, S. P. Ong, A. Banerjee, & Y. S. Meng. New insights into the interphase between the na metal anode and sulfide solid-state electrolytes: a joint experimental and computational study. *ACS Appl. Mater. Interfaces*, **10**, 10076–10086 (2018).

115. Y. Tian, Y. Sun, D. C. Hannah, Y. Xiao, H. Liu, K. W. Chapman, S.-H. Bo, & G. Ceder. Reactivity-guided interface design in Na metal solid-state batteries. *Joule*, **3**, 1037–1050 (2019).

116. Z. Deng, Z. Zhu, I.-H. Chu, & S. P. Ong. Data-driven first-principles methods for the study and design of alkali superionic conductors. *Chem. Mater.*, **29**, 281–288 (2017).

117. J. Auvergniot, A. Cassel, D. Foix, V. Viallet, V. Seznec, & R. Dedryvère. Redox activity of argyrodite Li_6PS_5Cl electrolyte in all-solid-state Li-ion battery: an XPS study. *Solid State Ionics*, **300**, 78–85 (2017).

118. J. Auvergniot, A. Cassel, J.-B. Ledeuil, V. Viallet, V. Seznec, & R. Dedryvre. Interface stability of argyrodite Li_6PS_5Cl toward $LiCoO_2$, $LiNi_{1/3}Co_{1/3}Mn_{1/3}O_2$, and $LiMn_2O_4$ in bulk all-solid-state batteries. *Chem. Mater.*, **29**, 3883–3890 (2017).

119. S. Wenzel, S. J. Sedlmaier, C. Dietrich, W. G. Zeier, & J. Janek. Interfacial reactivity and interphase growth of argyrodite solid electrolytes at lithium metal electrodes. *Solid State Ionics*, **318**, 102–112 (2018).

120. F. Walther, R. Koerver, T. Fuchs, S. Ohno, J. Sann, M. Rohnke, W. G. Zeier, & J. Janek. Visualization of the interfacial decomposition of composite cathodes in argyrodite based all-solid-state batteries using time-of-flight secondary ion mass spectrometry. *Chem. Mater.*, **31**, 3745–3755 (2019).

121. Z. Zhang, L. Zhang, X. Yan, H. Wang, Y. Liu, C. Yu, X. Cao, L. van Eijck, & B. Wen. All-in-one improvement toward Li_6PS_5Br-based solid electrolytes triggered by compositional tune. *J. Power Sources*, **410**, 162–170 (2019).

122. S. García-Martín, U. Amador, A. Morata-Orrantia, J. Rodríguez-Carvajal, & M. Á. Alario-Franco. Structure, microstructure, composition and properties of lanthanum lithium titanates and some substituted analogues. *Z. Anorg. Allg. Chem.*, **635**, 2363–2373 (2009).

123. C. Ma, K. Chen, C. Liang, C.-W. Nan, R. Ishikawa, K. More, & M. Chi. Atomic-scale origin of the large grain-boundary resistance in perovskite Li-ion-conducting solid electrolytes. *Energy Environ. Sci.*, **7**, 1638–1642 (2014).

124. S. Li, J. Zhu, Y. Wang, J. W. Howard, X. Lü, Y. Li, R. S. Kumar, L. Wang, L. L. Daemen, & Y. Zhao. Reaction mechanism studies towards effective fabrication of lithium-rich anti-perovskites Li_3OX (X = Cl, Br). *Solid State Ionics*, **284**, 14–19 (2016).

125. X. Xu, Z. Wen, J. Wu, & X. Yang. Preparation and electrical properties of NASICON-type structured $Li_{1.4}Al_{0.4}Ti_{1.6}(PO_4)_3$ glass-ceramics by the citric acid-assisted sol–gel method. *Solid State Ionics*, **178**, 29–34 (2007).

126. Y. Inaguma & M. Nakashima. A rechargeable lithium–air battery using a lithium ion-conducting lanthanum lithium titanate ceramics as an electrolyte separator. *J. Power Sources*, **228**, 250–255 (2013).

127. F. Schipper, E. M. Erickson, C. Erk, J.-Y. Shin, F. F. Chesneau, & D. Aurbach. Recent advances and remaining challenges for lithium ion battery cathodes I. Nickel-Rich, $LiNi_xCo_yMn_zO_2$. *J. Electrochem. Soc.*, **164**, A6220–A6228 (2017).

128. E. Antolini & M. Ferretti. Synthesis and thermal stability of $LiCoO_2$. *J. Solid State Chem.*, **117**, 1–7 (1995).

129. K. Park, B. C. Yu, J. W. Jung, Y. Li, W. Zhou, H. Gao, S. Son, & J. B. Goodenough. Electrochemical nature of the cathode interface for a solid-state lithium-ion battery: interface between $LiCoO_2$ and garnet-$Li_7La_3Zr_2O_{12}$. *Chem. Mater.*, **28**, 8051–8059 (2016).

130. S. Yu, A. Mertens, H. Tempel, R. Schierholz, H. Kungl, & R.-A. Eichel. Monolithic all-phosphate solid-state lithium-ion battery with improved interfacial compatibility. *ACS Appl. Mater. Interfaces*, **10**, 22264–22277 (2018).

131. T. Yoshinari, R. Koerver, P. Hofmann, Y. Uchimoto, W. G. Zeier, & J. Janek. Interfacial stability of phosphate-nasicon solid electrolytes in ni-rich ncm cathode-based solid-state batteries. *ACS Appl. Mater. Interfaces*, **11**, 23244–23253 (2019).

132. S. Qin, X. Zhu, Y. Jiang, M. Ling, Z. Hu, & J. Zhu. Growth of self-textured Ga^{3+}-substituted $Li_7La_3Zr_2O_{12}$ ceramics by solid state reaction and their significant enhancement in ionic conductivity. *Appl. Phys. Lett.*, **112**, 113901 (2018).

133. R. Murugan, W. Weppner, P. Schmid-Beurmann, & V. Thangadurai. Structure and lithium ion conductivity of bismuth containing lithium garnets $Li_5La_3Bi_2O_{12}$ and $Li_6SrLa_2Bi_2O_{12}$. *Mater. Sci. Eng. B*, **143**, 14–20 (2007).

134. R. Murugan, S. Ramakumar, & N. Janani. High conductive yttrium doped $Li_7La_3Zr_2O_{12}$ cubic lithium garnet. *Electrochem. Comm.*, **13**, 1373–1375 (2011).

135. V. Thangadurai, H. Kaack, & W. J. F. Weppner. Novel fast lithium ion conduction in garnet-type $Li_5La_3M_2O_2$ (M = Nb, Ta). *J. Am. Ceram. Soc.*, **86**, 437–440 (2003).

136. V. Thangadurai & W. Weppner. $Li_6ALa_2Ta_2O_{12}$ (A=Sr, Ba): novel garnet-like oxides for fast lithium ion conduction. *Adv. Funct. Mater.*, **15**, 107–112 (2005).

137. Y. Li, J.-T. Han, C.-A. Wang, H. Xie, & J. B. Goodenough. Optimizing Li^+ conductivity in a garnet framework. *J. Mater. Chem.*, **22**, 15357–15361 (2012).

138. A. Sharafi, S. Yu, M. Naguib, M. Lee, C. Ma, H. M. Meyer, J. Nanda, M. Chi, D. J. Siegel, & J. Sakamoto. Impact of air exposure and surface chemistry on Li–$Li_7La_3Zr_2O_{12}$ interfacial resistance. *J. Mater. Chem. A*, **5**, 13475–13487 (2017).

139. Y. Li, X. Chen, A. Dolocan, Z. Cui, S. Xin, L. Xue, H. Xu, K. Park, & J. B. Goodenough. Garnet electrolyte with an ultralow interfacial resistance for Li-metal batteries. *J. Am. Chem. Soc.*, **140**, 6448–6455 (2018).

140. J. Dai, C. Yang, C. Wang, G. Pastel, & L. Hu. Interface engineering for garnet-based solid-state lithium-metal batteries: materials, structures, and characterization. *Adv. Mater.*, **30**, 1802068 (2018).

141. K. Hofstetter, A. J. Samson, S. Narayanan, & V. Thangadurai. Present understanding of the stability of Li-stuffed garnets with moisture, carbon dioxide, and metallic lithium. *J. Power Sources*, **390**, 297–312 (2018).

142. R. Jalem, Y. Morishita, T. Okajima, H. Takeda, Y. Kondo, M. Nakayama, & T. Kasuga. Experimental and first-principles DFT study on the electrochemical reactivity of garnet-type solid electrolytes with carbon. *J. Mater. Chem. A*, **4**, 14371–14379 (2016).

143. L. J. Miara, W. D. Richards, Y. E. Wang, & G. Ceder. First-principles studies on cation dopants and electrolyte—cathode interphases for lithium garnets. *Chem. Mater.*, **27**, 4040–4047 (2015).

144. M. Kotobuki, K. Kanamura, Y. Sato, & T. Yoshida. Fabrication of all-solid-state lithium battery with lithium metal anode using Al_2O_3-added $Li_7La_3Zr_2O_{12}$ solid electrolyte. *J. Power Sources*, **196**, 7750–7754 (2011).

145. M. Kotobuki & K. Kanamura. Fabrication of all-solid-state battery using $Li_5La_3Ta_2O_{12}$ ceramic electrolyte. *Ceram. Int.*, **39**, 6481–6487 (2013).

146. E. Rangasamy, G. Sahu, J. K. Keum, A. J. Rondinone, N. J. Dudney, & C. Liang. A high conductivity oxide–sulfide composite lithium superionic conductor. *J. Mater. Chem. A*, **2**, 4111–4116 (2014).

147. M. Nakayama, M. Kotobuki, H. Munakata, M. Nogami, & K. Kanamura. First-principles density functional calculation of electrochemical stability of fast Li ion conducting garnet-type oxides. *Phys. Chem. Chem. Phys.*, **14**, 10008–10014 (2012).

148. Y. Li, C.-A. Wang, H. Xie, J. Cheng, & J. B. Goodenough. High lithium ion conduction in garnet-type $Li_6La_3ZrTaO_{12}$. *Electrochem. Comm.*, **13**, 1289–1292 (2011).

149. H. Nemori, Y. Matsuda, S. Mitsuoka, M. Matsui, O. Yamamoto, Y. Takeda, & N. Imanishi. Stability of garnet-type solid electrolyte $Li_xLa_3A_{2-y}B_yO_{12}$ (A = Nb or Ta, B = Sc or Zr). *Solid State Ionics*, **282**, 7–12 (2015).

150. Y. Kim, A. Yoo, R. Schmidt, A. Sharafi, H. Lee, J. Wolfenstine, & J. Sakamoto. Electrochemical stability of $Li_{6.5}La_3Zr_{1.5}M_{0.5}O_{12}$ (M= Nb or Ta) against metallic lithium. *Front. Energy Res.*, **4**, 20 (2016).

151. L. Cheng, J. S. Park, H. Hou, V. Zorba, G. Chen, T. Richardson, J. Cabana, R. Russo, & M. Doeff. Effect of microstructure and surface impurity segregation on the electrical and electrochemical properties of dense Al-substituted $Li_7La_3Zr_2O_{12}$. *J. Mater. Chem. A*, **2**, 172–181 (2014).

152. X. Yan, Z. Li, H. Ying, F. Nie, L. Xue, Z. Wen, & W.-Q. Han. A novel thin solid electrolyte film and its application in all-solid-state battery at room temperature. *Ionics*, **24**, 1545–1551 (2018).

153. M. Fingerle, C. Loho, T. Ferber, H. Hahn, & R. Hausbrand. Evidence of the chemical stability of the garnet-type solid electrolyte $Li_5La_3Ta_2O_{12}$ towards lithium by a surface science approach. *J. Power Sources*, **366**, 72–79 (2017).

154. J. Wolfenstine, J. L. Allen, J. Read, & J. Sakamoto. Chemical stability of cubic $Li_7La_3Zr_2O_{12}$ with molten lithium at elevated temperature. *J. Mater. Sci.*, **48**, 5846–5851 (2013).

155. C. Ma, Y. Cheng, K. Yin, J. Luo, A. Sharafi, J. Sakamoto, J. Li, K. L. More, N. J. Dudney, & M. Chi. Interfacial stability of Li metal-solid electrolyte elucidated via in situ electron microscopy. *Nano Lett.*, **16**, 7030–7036 (2016).

156. Y. Zhu, J. G. Connell, S. Tepavcevic, P. Zapol, R. Garcia-Mendez, N. J. Taylor, J. Sakamoto, B. J. Ingram, L. A. Curtiss, J. W. Freeland, et al. Dopant-dependent stability of garnet solid electrolyte interfaces with lithium metal. *Adv. Energy Mater.*, **9**, 1803440 (2019).

157. D. Rettenwander, R. Wagner, A. Reyer, M. Bonta, L. Cheng, M. M. Doeff, A. Limbeck, M. Wilkening, & G. Amthauer. Interface instability of Fe-stabilized $Li_7La_3Zr_2O_{12}$ versus Li metal. *J. Phys. Chem. C*, **122**, 3780–3785 (2018).

158. S. Afyon, F. Krumeich, & J. L. Rupp. A shortcut to garnet-type fast Li-ion conductors for all-solid state batteries. *J. Mater. Chem. A*, **3**, 18636–18648 (2015).

159. S. P. Ong, L. Wang, B. Kang, & G. Ceder. Li-Fe-P-O_2 phase diagram from first principles calculations. *Chem. Mater.*, **20**, 1798–1807 (2008).

160. E. Yi, W. Wang, J. Kieffer, & R. M. Laine. Flame made nanoparticles permit processing of dense, flexible, Li^+ conducting ceramic electrolyte thin films of cubic-$Li_7La_3Zr_2O_{12}$ (c-LLZO). *J. Mater. Chem. A*, **4**, 12947–12954 (2016).

161. Y. Ren, T. Liu, Y. Shen, Y. Lin, & C.-W. Nan. Chemical compatibility between garnet-like solid state electrolyte $Li_{6.75}La_3Zr_{1.75}Ta_{0.25}O_{12}$ and major commercial lithium battery cathode materials. *Journal of Materiomics*, **2**, 256–264 (2016).

162. V. Thangadurai & W. Weppner. Investigations on electrical conductivity and chemical compatibility between fast lithium ion conducting garnet-like $Li_6BaLa_2Ta_2O_{12}$ and lithium battery cathodes. *J. Power Sources*, **142**, 339–344 (2005).

163. C.-L. Tsai, Q. Ma, C. Dellen, S. Lobe, F. Vondahlen, A. Windmüller, D. Grüner, H. Zheng, S. Uhlenbruck, M. Finsterbusch, et al. A garnet structure-based all-solid-state Li battery without interface modification: resolving incompatibility issues on positive electrodes. *Sustainable Energy & Fuels*, **3**, 280–291 (2019).

164. M. Bitzer, T. Van Gestel, S. Uhlenbruck, et al. Sol-gel synthesis of thin solid $Li_7La_3Zr_2O_{12}$ electrolyte films for Li-ion batteries. *Thin Solid Films*, **615**, 128–134 (2016).

165. G. Vardar, W. J. Bowman, Q. Lu, J. Wang, R. J. Chater, A. Aguadero, R. Seibert, J. Terry, A. Hunt, I. Waluyo, et al. Structure, chemistry, and charge transfer resistance of the interface between $Li_7La_3Zr_2O_{12}$ electrolyte and $LiCoO_2$ cathode. *Chem. Mater.*, **30**, 6259–6276 (2018).

166. B. L. Ellis, K. T. Lee, & L. F. Nazar. Positive electrode materials for Li-ion and Li-batteries. *Chem. Mater.*, **22**, 691–714 (2010).

167. S. Ohta, T. Kobayashi, J. Seki, & T. Asaoka. Electrochemical performance of an all-solid-state lithium ion battery with garnet-type oxide electrolyte. *J. Power Sources*, **202**, 332–335 (2012).

168. X. Ma, B. Kang, & G. Ceder. High rate micron-sized ordered $LiNi_{0.5}Mn_{1.5}O_4$. *J. Electrochem. Soc.*, **157**, A925–A931 (2010).

169. A. Manthiram, K. Chemelewski, & E.-S. Lee. A perspective on the high-voltage $LiMn_{1.5}Ni_{0.5}O_4$ spinel cathode for lithium-ion batteries. *Energy Environ. Sci.*, **7**, 1339–1350 (2014).

170. J. B. Bates, N. J. Dudney, G. R. Gruzalski, R. A. Zuhr, A. Choudhury, C. F. Luck, & J. D. Robertson. Fabrication and characterization of amorphous lithium electrolyte thin films and rechargeable thin-film batteries. *J. Power Sources*, **43**, 103–110 (1993).

171. N. Suzuki, S. Shirai, N. Takahashi, T. Inaba, & T. Shiga. A lithium phosphorous oxynitride (LiPON) film sputtered from unsintered Li_3PO_4 powder target. *Solid State Ionics*, **191**, 49–54 (2011).

172. J. Li, N. J. Dudney, J. Nanda, & C. Liang. Artificial solid electrolyte interphase to address the electrochemical degradation of silicon electrodes. *ACS Appl. Mater. Interfaces*, **6**, 10083–10088 (2014).

173. L. Le Van-Jodin, F. Ducroquet, F. Sabary, & I. Chevalier. Dielectric properties, conductivity and Li^+ ion motion in LiPON thin films. *Solid State Ionics*, **253**, 151–156 (2013).

174. J. B. Bates, N. J. Dudney, B. Neudecker, A. Ueda, & C. D. Evans. Thin-film lithium and lithium-ion batteries. *Solid State Ionics*, **135**, 33–45 (2000).

175. U. V. Alpen, A. Rabenau, & G. H. Talat. Ionic conductivity in Li_3N single crystals. *Appl. Phys. Lett.*, **30**, 621–623 (1977).

176. G. Nazri. Preparation, structure and ionic conductivity of lithium phosphide. *Solid State Ionics*, **34**, 97–102 (1989).

177. M. Fingerle, R. Buchheit, S. Sicolo, K. Albe, & R. Hausbrand. Reaction and space charge layer formation at the $LiCoO_2$–LiPON interface: insights on defect formation and ion energy level alignment by a combined surface science–simulation approach. *Chem. Mater.*, **29**, 7675–7685 (2017).

178. Z. Wang, D. Santhanagopalan, W. Zhang, F. Wang, H. L. Xin, K. He, J. Li, N. Dudney, & Y. S. Meng. In situ STEM-EELS observation of nanoscale interfacial phenomena in all-solid-state batteries. *Nano Lett.*, **16**, 3760–3767 (2016).

179. Y. Inaguma, C. Liquan, M. Itoh, T. Nakamura, T. Uchida, H. Ikuta, & M. Wakihara. High ionic conductivity in lithium lanthanum titanate. *Solid State Commun.*, **86**, 689–693 (1993).

180. C. Chen & K. Amine. Ionic conductivity, lithium insertion and extraction of lanthanum lithium titanate. *Solid State Ionics*, **144**, 51–57 (2001).

181. Y. J. Shan, L. Chen, Y. Inaguma, M. Itoh, & T. Nakamura. Oxide cathode with perovskite structure for rechargeable lithium batteries. *J. Power Sources*, **54**, 397–402 (1995).

182. O. Bohnke, C. Bohnke, & J. Fourquet. Mechanism of ionic conduction and electrochemical intercalation of lithium into the perovskite lanthanum lithium titanate. *Solid State Ionics*, **91**, 21–31 (1996).

183. M. Nakayama, T. Usui, Y. Uchimoto, M. Wakihara, & M. Yamamoto. Changes in electronic structure upon lithium insertion into the A-site deficient perovskite type oxides (Li, La) TiO_3. *J. Phys. Chem. B*, **109**, 4135–4143 (2005).

184. Z. Jiang, H. Xie, S. Wang, X. Song, X. Yao, & H. Wang. Perovskite membranes with vertically aligned microchannels for all-solid-state lithium batteries. *Adv. Energy Mater.*, **8**, 1801433 (2018).

185. K. Kishida, N. Wada, H. Adachi, K. Tanaka, H. Inui, C. Yada, Y. Iriyama, & Z. Ogumi. Microstructure of the $LiCoO_2$ (cathode)/$La_{2/3-x}Li_{3x}TiO_3$ (electrolyte) interface and its influences on the electrochemical properties. *Acta materialia*, **55**, 4713–4722 (2007).

186. C.-L. Liao, C.-H. Wen, & K.-Z. Fung. The stability between perovskite $La_{2/3-x}Li_{3x}\square_{1/3-2x}TiO_3$ (3x=0.3) electrolyte and LiM_mO_n (M= Mn, Ni and Co) cathodes. *J. Alloys Compd.*, **432**, L22–L25 (2007).

187. M. Kotobuki, Y. Suzuki, H. Munakata, K. Kanamura, Y. Sato, K. Yamamoto, & T. Yoshida. Compatibility of $LiCoO_2$ and $LiMn_2O_4$ cathode materials for $Li_{0.55}La_{0.35}TiO_3$ electrolyte to fabricate all-solid-state lithium battery. *J. Power Sources*, **195**, 5784–5788 (2010).

188. X. Lü, G. Wu, J. W. Howard, A. Chen, Y. Zhao, L. L. Daemen, & Q. Jia. Li-rich anti-perovskite Li_3OCl films with enhanced ionic conductivity. *Chem. Commun.*, **50**, 11520–11522 (2014).

189. X. Lü, J. W. Howard, A. Chen, J. Zhu, S. Li, G. Wu, P. Dowden, H. Xu, Y. Zhao, & Q. Jia. Antiperovskite Li_3OCl superionic conductor films for solid-state Li-ion batteries. *Adv. Sci.*, **3**, 1500359 (2016).

190. A. Emly, E. Kioupakis, & A. Van der Ven. Phase stability and transport mechanisms in antiperovskite Li_3OCl and Li_3OBr superionic conductors. *Chem. Mater.*, **25**, 4663–4670 (2013).

191. Y. Zhang, Y. Zhao, & C. Chen. Ab initio study of the stabilities of and mechanism of superionic transport in lithium-rich antiperovskites. *Phys. Rev. B*, **87**, 134303 (2013).

192. M.-H. Whangbo, H.-J. Koo, A. Villesuzanne, & M. Pouchard. Effect of metal-oxygen covalent bonding on the competition between Jahn-Teller distortion and charge disproportionation in the perovskites of high-spin d4 metal ions $LaMnO_3$ and $CaFeO_3$. *Inorg. Chem.*, **41**, 1920–1929 (2002).

193. M. H. Braga, J. A. Ferreira, V. Stockhausen, J. E. Oliveira, & A. El-Azab. Novel Li_3ClO based glasses with superionic properties for lithium batteries. *J. Mater. Chem. A*, **2**, 5470–5480 (2014).

194. Y. Li, W. Zhou, S. Xin, S. Li, J. Zhu, L. Xujie, Z. Cui, Q. Jia, J. Zhou, Y. Zhao, & J. B. Goodenough. Fluorine-doped antiperovskite electrolyte for all-solid-state lithium-ion batteries. *Angew. Chem. Int. Ed.*, **55**, 9965–9968 (2016).

195. N. Anantharamulu, K. K. Rao, G. Rambabu, B. V. Kumar, V. Radha, & M. Vithal. A wide-ranging review on Nasicon type materials. *J. Mater. Sci.*, **46**, 2821–2837 (2011).

196. J. Fu. Fast Li^+ ion conducting glass-ceramics in the system Li_2O–Al_2O_3–GeO_2–P_2O_5. *Solid State Ionics*, **104**, 191–194 (1997).

197. K. Arbi, W. Bucheli, R. Jiménez, & J. Sanz. High lithium ion conducting solid electrolytes based on NASICON $Li_{1+x}Al_xM_{2-x}(PO_4)_3$ materials (M= Ti, Ge and 0≥x≥0.5). *J. Eur. Ceram. Soc.*, **35**, 1477–1484 (2015).

198. J. Feng, L. Lu, & M. Lai. Lithium storage capability of lithium ion conductor $Li_{1.5}Al_{0.5}Ge_{1.5}(PO_4)_3$. *J. Alloys Compd.*, **501**, 255–258 (2010).

199. P. Hartmann, T. Leichtweiss, M. R. Busche, M. Schneider, M. Reich, J. Sann, P. Adelhelm, & J. Janek. Degradation of NASICON-type materials in contact with lithium metal: formation of mixed conducting interphases (MCI) on solid electrolytes. *J. Phys. Chem. C*, **117**, 21064–21074 (2013).

200. B. Wu, S. Wang, J. Lochala, D. Desrochers, B. Liu, W. Zhang, J. Yang, & J. Xiao. The role of the solid electrolyte interphase layer in preventing Li dendrite growth in solid-state batteries. *Energy Environ. Sci.*, **11**, 1803–1810 (2018).

201. L. He, Q. Sun, C. Chen, J. A. S. Oh, J. Sun, M. Li, W. Tu, H.-H. Zhou, K. Zeng, & L. Lu. Failure mechanism and interface engineering for nasicon structure all-solid-state lithium metal batteries. *ACS Appl. Mater. Interfaces*, **11**, 20895–20904 (2019).

202. J. A. Lewis, F. J. Q. Cortes, M. G. Boebinger, J. Tippens, T. S. Marchese, N. P. Kondekar, X. Liu, M. Chi, & M. T. McDowell. Interphase morphology between a solid-state electrolyte and lithium controls cell failure. *ACS Energy Lett.*, **4**, 591–599 (2019).

203. J. Tippens, J. Miers, A. Afshar, J. Lewis, F. J. Q. Cortes, H. Qiao, T. S. Marchese, C. V. Di Leo, C. Saldana, & M. T. McDowell. Visualizing chemo-mechanical degradation of a solid-state battery electrolyte. *ACS Energy Lett.*, **4**, 1475–1483 (2019).

204. X. Xu, Z. Wen, X. Wu, X. Yang, & Z. Gu. Lithium ion-conducting glass–ceramics of $Li_{1.5}Al_{0.5}Ge_{1.5}(PO_4)_3$–$xLi_2O$ (x= 0.0–0.20) with good electrical and electrochemical properties. *J. Am. Ceram. Soc.*, **90**, 2802–2806 (2007).

205. H.-S. Kim, Y. Oh, K. H. Kang, J. H. Kim, J. Kim, & C. S. Yoon. Characterization of sputter-deposited $LiCoO_2$ thin film grown on NASICON-type electrolyte for application in all-solid-state rechargeable lithium battery. *ACS Appl. Mater. Interfaces*, **9**, 16063–16070 (2017).

206. Y. Li, W. Zhou, X. Chen, X. Lü, Z. Cui, S. Xin, L. Xue, Q. Jia, & J. B. Goodenough. Mastering the interface for advanced all-solid-state lithium rechargeable batteries. *Proc. Natl. Acad. Sci. USA*, **113**, 13313–13317 (2016).

207. H. El-Shinawi, A. Regoutz, D. J. Payne, E. J. Cussen, & S. A. Corr. NASICON $LiM_2(PO_4)_3$ electrolyte (M= Zr) and electrode (M= Ti) materials for all solid-state Li-ion batteries with high total conductivity and low interfacial resistance. *J. Mater. Chem. A*, **6**, 5296–5303 (2018).

208. T. Kato, T. Hamanaka, K. Yamamoto, T. Hirayama, F. Sagane, M. Motoyama, & Y. Iriyama. In-situ $Li_7La_3Zr_2O_{12}$/$LiCoO_2$ interface modification for advanced all-solid-state battery. *J. Power Sources*, **260**, 292–298 (2014).

209. Y. Kim, G. M. Veith, J. Nanda, R. R. Unocic, M. Chi, & N. J. Dudney. High voltage stability of $LiCoO_2$ particles with a nano-scale Lipon coating. *Electrochim. Acta*, **56**, 6573–6580 (2011).

210. J. Song, S. Jacke, D. Becker, R. Hausbrand, & W. Jaegermann. Stabilization of thin film $LiCoO_2$ electrode by LiPON coating. *Electrochem. Solid-State Lett.*, **14**, A11–A13 (2011).

211. S. K. Martha, J. Nanda, Y. Kim, R. R. Unocic, S. Pannala, & N. J. Dudney. Solid electrolyte coated high voltage layered–layered lithium-rich composite cathode: $Li_{1.2}Mn_{0.525}Ni_{0.175}Co_{0.1}O_2$. *J. Mater. Chem. A*, **1**, 5587–5595 (2013).

212. X. Li, L. Jin, D. Song, H. Zhang, X. Shi, Z. Wang, L. Zhang, & L. Zhu. $LiNbO_3$-coated $LiNi_{0.8}Co_{0.1}Mn_{0.1}O_2$ cathode with high discharge capacity and rate performance for all-solid-state lithium battery. *J. Energy Chem.*, **40**, 39–45 (2020).

213. S. Ito, S. Fujiki, T. Yamada, Y. Aihara, Y. Park, T. Y. Kim, S.-W. Baek, J.-M. Lee, S. Doo, & N. Machida. A rocking chair type all-solid-state lithium ion battery adopting Li_2O–ZrO_2 coated $LiNi_{0.8}Co_{0.15}Al_{0.05}O_2$ and a sulfide based electrolyte. *J. Power Sources*, **248**, 943–950 (2014).

214. A. Sakuda, H. Kitaura, A. Hayashi, K. Tadanaga, & M. Tatsumisago. Improvement of high-rate performance of all-solid-state lithium secondary batteries using $LiCoO_2$ coated with Li_2O–SiO_2 glasses. *Electrochem. Solid-State Lett.*, **11**, A1–A3 (2008).

215. Y. Sakurai, A. Sakuda, A. Hayashi, & M. Tatsumisago. Preparation of amorphous Li_4SiO_4–Li_3PO_4 thin films by pulsed laser deposition for all-solid-state lithium secondary batteries. *Solid State Ionics*, **182**, 59–63 (2011).

216. S. H. Jung, K. Oh, Y. J. Nam, D. Y. Oh, P. Brner, K. Kang, & Y. S. Jung. Li_3BO_3–Li_2CO_3: rationally designed buffering phase for sulfide all-solid-state Li-ion batteries. *Chem. Mater.*, **30**, 8190–8200 (2018).

217. K. Chen, K. Yamamoto, Y. Orikasa, T. Uchiyama, Y. Ito, S. Yubuchi, A. Hayashi, M. Tatsumisago, K. Nitta, T. Uruga, et al. Effect of introducing interlayers into electrode/electrolyte interface in all-solid-state battery using sulfide electrolyte. *Solid State Ionics*, **327**, 150–156 (2018).

218. H. W. Kwak & Y. J. Park. Cathode coating using $LiInO_2$-LiI composite for stable sulfide-based all-solid-state batteries. *Sci. Rep.*, **9**, 8099 (2019).

219. H. W. Kwak & Y. J. Park. Li_2MoO_4 coated Ni-rich cathode for all-solid-state batteries. *Thin Solid Films*, **660**, 625–630 (2018).

220. S. Ohta, S. Komagata, J. Seki, T. Saeki, S. Morishita, & T. Asaoka. All-solid-state lithium ion battery using garnet-type oxide and Li_3BO_3 solid electrolytes fabricated by screen-printing. *J. Power Sources*, **238**, 53–56 (2013).

221. L. Sang, K. L. Bassett, F. C. Castro, M. J. Young, L. Chen, R. T. Haasch, J. W. Elam, V. P. Dravid, R. G. Nuzzo, & A. A. Gewirth. Understanding the effect of interlayers at the thiophosphate solid electrolyte/lithium interface for all-solid-state li batteries. *Chem. Mater.*, **30**, 8747–8756 (2018).

222. Y. Liu, Q. Sun, Y. Zhao, B. Wang, P. Kaghazchi, K. R. Adair, R. Li, C. Zhang, J. Liu, L.-Y. Kuo, et al. Stabilizing the interface of nasicon solid electrolyte against Li metal with atomic layer deposition. *ACS Appl. Mater. Interfaces*, **10**, 31240–31248 (2018).

223. Y. Ruan, Y. Lu, X. Huang, J. Su, C. Sun, J. Jin, & Z. Wen. Acid induced conversion towards robust and lithiophilic interface for Li-$Li_7La_3Zr_2O_{12}$ solid-state battery. *J. Mater. Chem. A*, **7**, 14565–14574 (2019).

224. Z. Zhang, S. Chen, J. Yang, J. Wang, L. Yao, X. Yao, P. Cui, & X. Xu. Interface re-engineering of $Li_{10}GeP_2S_{12}$ electrolyte and lithium anode for all-solid-state lithium batteries with ultralong cycle life. *ACS Appl. Mater. Interfaces*, **10**, 2556–2565 (2018).

225. Y. Zhu, X. He, & Y. Mo. Strategies based on nitride materials chemistry to stabilize Li metal anode. *Adv. Sci.*, **4**, 1600517 (2017).

226. Q. Cheng, A. Li, N. Li, S. Li, A. Zangiabadi, W. Huang, A. C. Li, T. Jin, Q. Song, W. Xu, et al. Stabilizing solid electrolyte-anode interface in Li-metal batteries by boron nitride-based nanocomposite coating. *Joule*, **3**, 1510–1522 (2019).

227. M. Shigeno, K. Nagao, M. Deguchi, C. Hotehama, H. Kowada, A. Sakuda, A. Hayashi, & M. Tatsumisago. New lithium-conducting nitride glass Li_3BN_2. *Solid State Ionics*, **339**, 114985 (2019).

228. Y. Wang, W. D. Richards, S.-H. Bo, L. J. Miara, & G. Ceder. Computational prediction and evaluation of solid-state sodium superionic conductors $Na_7P_3X_{11}$ (X= O, S, Se). *Chem. Mater.*, **29**, 7475–7482 (2017).

229. S. Muy, J. C. Bachman, L. Giordano, H.-H. Chang, D. L. Abernathy, D. Bansal, O. Delaire, S. Hori, R. Kanno, F. Maglia, et al. Tuning mobility and stability of lithium ion conductors based on lattice dynamics. *Energy Environ. Sci.*, **11**, 850–859 (2018).

230. S. Wang, Q. Bai, A. M. Nolan, Y. Liu, S. Gong, Q. Sun, & Y. Mo. Lithium chlorides and bromides as promising solid-state chemistries for fast ion conductors with good electrochemical stability. *Angew. Chem. Int. Ed.*, **58**, 8039–8043 (2019).

231. T. Asano, A. Sakai, S. Ouchi, M. Sakaida, A. Miyazaki, & S. Hasegawa. Solid halide electrolytes with high lithium-ion conductivity for application in 4 V class bulk-type all-solid-state batteries. *Adv. Mater.*, **30**, 1803075 (2018).

232. X. Li, J. Liang, J. Luo, M. N. Banis, C. Wang, W. Li, S. Deng, C. Yu, F. Zhao, Y. Hu, et al. Air-stable Li_3InCl_6 electrolyte with high voltage compatibility for all-solid-state batteries. *Energy Environ. Sci.*, **12**, 2665–2671 (2019).

233. T. Krauskopf, S. P. Culver, & W. G. Zeier. Bottleneck of diffusion and inductive effects in $Li_{10}Ge_{1-x}Sn_xP_2S_{12}$. *Chem. Mater.*, **30**, 1791–1798 (2018).

234. A. M. Nolan, Y. Zhu, X. He, Q. Bai, & Y. Mo. Computation-accelerated design of materials and interfaces for all-solid-state lithium-ion batteries. *Joule*, **2**, 2016–2046 (2018).

235. A. D. Sendek, Q. Yang, E. D. Cubuk, K.-A. N. Duerloo, Y. Cui, & E. J. Reed. Holistic computational structure screening of more than 12000 candidates for solid lithium-ion conductor materials. *Energy Environ. Sci.*, **10**, 306–320 (2017).

236. A. Pradel & M. Ribes. Lithium chalcogenide conductive glasses. *Mater. Chem. Phys.*, **23**, 121–142 (1989).

237. L. Duchêne, R.-S. Kühnel, D. Rentsch, A. Remhof, H. Hagemann, & C. Battaglia. A highly stable sodium solid-state electrolyte based on a dodeca/deca-borate equimolar mixture. *Chem. Commun.*, **53**, 4195–4198 (2017).

238. Y. Sadikin, M. Brighi, P. Schouwink, & R. Černỳ. Superionic conduction of sodium and lithium in anion-mixed hydroborates $Na_3BH_4B_{12}H_{12}$ and $(Li_{0.7}Na_{0.3})_3BH_4B_{12}H_{12}$. *Adv. Energy Mater.*, **5**, 1501016 (2015).

239. G. Dewald, S. Ohno, M. Kraft, R. Koerver, P. Till, N. Vargas, J. Janek, & W. Zeier. Experimental assessment of the practical oxidative stability of lithium thiophosphate solid electrolytes. *ChemRxiv*, (2019).

240. S. Hori, K. Suzuki, M. Hirayama, Y. Kato, T. Saito, M. Yonemura, & R. Kanno. Synthesis, structure, and ionic conductivity of solid solution, $Li_{10+\delta}M_{1+\delta}P_{2-\delta}S_{12}$ (M= Si, Sn). *Faraday Discuss.*, **176**, 83–94 (2015).

241. N. Elgrishi, K. J. Rountree, B. D. McCarthy, E. S. Rountree, T. T. Eisenhart, & J. L. Dempsey. A practical beginner's guide to cyclic voltammetry. *J. Chem. Educ.*, **95**, 197–206 (2017).

242. C. Yu, J. Hageman, S. Ganapathy, L. van Eijck, L. Zhang, K. R. Adair, X. Sun, & M. Wagemaker. Tailoring Li_6PS_5Br ionic conductivity and understanding of its role in cathode mixtures for high performance all-solid-state Li–S batteries. *J. Mater. Chem. A*, **7**, 10412–10421 (2019).

243. A. Smith, J. Burns, & J. Dahn. A high precision study of the coulombic efficiency of Li-ion batteries. *Electrochem. Solid-State Lett.*, **13**, A177–A179 (2010).

244. A. Smith, J. Burns, S. Trussler, & J. Dahn. Precision measurements of the coulombic efficiency of lithium-ion batteries and of electrode materials for lithium-ion batteries. *J. Electrochem. Soc.*, **157**, A196–A202 (2010).

245. P. Meister, H. Jia, J. Li, R. Kloepsch, M. Winter, & T. Placke. Best practice: performance and cost evaluation of lithium ion battery active materials with special emphasis on energy efficiency. *Chem. Mater.*, **28**, 7203–7217 (2016).

246. S. Farhad & A. Nazari. Introducing the energy efficiency map of lithium-ion batteries. *Int. J. Energy Res.*, **43**, 931–944 (2019).

247. Y. Wang, W. D. Richards, S. P. Ong, L. J. Miara, J. C. Kim, Y. Mo, & G. Ceder. Design principles for solid-state lithium superionic conductors. *Nat. Mater.*, **14**, 1026–1031 (2015).

248. X. He, Y. Zhu, & Y. Mo. Origin of fast ion diffusion in super-ionic conductors. *Nat. Commun.*, **8**, 15893 (2017).

249. S. Xiong, X. He, A. Han, Z. Liu, Z. Ren, B. McElhenny, A. M. Nolan, S. Chen, Y. Mo, & H. Chen. Computation-guided design of $LiTaSiO_5$, a new lithium ionic conductor with sphene structure. *Adv. Energy Mater.*, **9**, 1803821 (2019).

250. A. Jain, G. Hautier, C. J. Moore, S. P. Ong, C. C. Fischer, T. Mueller, K. A. Persson, & G. Ceder. A high-throughput infrastructure for density functional theory calculations. *Comput. Mater. Sci.*, **50**, 2295–2310 (2011).

251. S. Curtarolo, G. L. Hart, M. B. Nardelli, N. Mingo, S. Sanvito, & O. Levy. The high-throughput highway to computational materials design. *Nat. Mater.*, **12**, 191–201 (2013).